



1 **Real-Time Snow Depth Estimation and Historical Data**  
2 **Reconstruction Over China Based on a Random Forest**  
3 **Machine Learning Approach**  
4

5 Jianwei Yang<sup>1</sup>, Lingmei Jiang<sup>1</sup>, Kari Luojus<sup>2</sup>, Jinmei Pan<sup>3</sup>, Juha Lemmetyinen<sup>2</sup>,  
6 Matias Takala<sup>2</sup>, Shengli Wu<sup>4</sup>

7 <sup>1</sup>State Key Laboratory of Remote Sensing Science, Jointly Sponsored by Beijing Normal University and  
8 the Institute of Remote Sensing and Digital Earth of Chinese Academy of Sciences, Beijing Engineering  
9 Research Center for Global Land Remote Sensing Products, Faculty of Geographical Science, Beijing  
10 Normal University, Beijing 100875, China

11 <sup>2</sup>Finnish Meteorological Institute, Helsinki Fi00101, Finland

12 <sup>3</sup>State Key Laboratory of Remote Sensing Science, Institute of Remote Sensing and Digital Earth,  
13 Chinese Academy of Sciences, Beijing 100101, China

14 <sup>4</sup>National Satellite Meteorological Center, China Meteorological Administration, Beijing 100081, China

15 *Corresponding Author:* Lingmei Jiang (jiang@bnu.edu.cn)

16 **Abstract.** Snow depth data time series are valuable for climatological and hydrological applications.  
17 Passive microwave (PMW) sensors are advantageous for estimating spatially and temporally continuous  
18 snow depth. However, PMW estimate accuracy has several problems, which results in poor performances  
19 of traditional snow depth estimation algorithms. Machine learning (ML) is a common method used in  
20 many research fields, and its early application in remote sensing is promising. In this study, we propose  
21 a new and accurate approach based on the ML technique to estimate real-time snow depth and reconstruct  
22 historical snow depth from 1987-2018. First, we trained the random forest (RF) model with advanced  
23 microwave scanning radiometer 2 (AMSR2) brightness temperatures ( $T_B$ ) at 10.65, 18.7, 36.5 and 89  
24 GHz, land cover fraction (forest, shrub, grass, farm and barren), geolocation (latitude and longitude) and  
25 station observation from 2014-2015. Then, the trained RF model was used to retrieve a reference dataset  
26 with 2012-2018 AMSR2  $T_B$  data as the accurate snow depth. With this reference snow depth dataset, we  
27 developed the pixel-based algorithm for the Special Sensor Microwave/Imager (SSM/I) and Special  
28 Sensor Microwave Imager Sounder (SSMIS). Finally, the pixel-based method was used to reconstruct a  
29 consistent 31-year daily snow depth dataset for 1987-2018. We validated the trained RF model using the  
30 weather station observations and AMSR2  $T_B$  during 2012-2013. The results showed that the RF model  
31 root mean square error (RMSE) and bias were 4.5 cm and 0.04 cm, respectively. The pixel-based



1 algorithm's accuracy was evaluated against the field sampling experiments dataset (January-March, 2018)  
2 and station observations in 2017-2018, and the RMSEs were 2.0 cm and 5.1 cm, respectively. The pixel-  
3 based method performs better than the previous regression method fitted in China (RMSEs are 4.7 cm  
4 and 8.4 cm, respectively). The high accuracy of the pixel-based method can be attributed to the spatial  
5 dynamic retrieval coefficients and accurate snow depth estimates of the RF model. Additionally, the  
6 1987-2018 long-term snow depth dataset was analyzed in terms of temporal and spatial variations. On  
7 the spatial scale, daily maximum snow depth tends to occur in Xinjiang and the Himalayas during 1992-  
8 2018. However, the daily mean snow depth in Northeast China is the largest. For the temporal  
9 characteristics, the February mean snow depth is the thickest during snowy winter seasons. Interestingly,  
10 the January mean snow depth represents the annual mean snow depth, which plays an important role in  
11 snow depth prediction and hydrological management. In conclusion, through step-by-step validation  
12 using in situ observations, our pixel-based approach is available in real-time snow depth retrievals and  
13 historical data reconstruction.

## 14 **1 Introduction**

15 Seasonal snow cover is an important parameter in the context of the Earth's hydrological cycle, the global  
16 radiation balance, and climate system (Fernandes et al., 2009; Hernández-Henríquez et al., 2015; Derksen  
17 et al., 2012; Kevin et al., 2017; Huss et al., 2017; Dorji et al., 2018). The latest Intergovernmental Panel  
18 on Climate Change (IPCC) special report of 2018 stated that the cryosphere is very sensitive to climatic  
19 changes, and extreme snow cover changes and melting caused by global warming were threatening  
20 natural and human systems (Hoegh-Guldberg et al., 2018). Long-term snow cover records are crucial for  
21 climate studies, hydrological applications and weather forecasts over the Northern Hemisphere (Gong et  
22 al., 2007; Derksen et al., 2012; Safavi et al., 2017; Tedesco et al., 2016; Huang et al., 2017; Zhong et al.,  
23 2018). A key parameter is the snow water equivalent (SWE), which describes the amount of water stored  
24 in the snowpack as a product of snow depth and mean snow density (Dressler et al., 2006; Kelly et al.,  
25 2009; Foster et al., 2011; Xiao et al., 2018; Takala et al., 2017; Tedesco et al., 2016). Fortunately, passive  
26 microwave (PMW) signals can penetrate snow cover and provide snow depth estimates through volume  
27 scattering of snow particles in dry snow conditions. PMW remote sensing also has the advantage of  
28 sensing without the dependency of solar illumination and weather conditions (Chang et al., 1987; Foster



1 et al., 2011; Larue et al., 2017). In addition, there exists a long achieved historical spaceborne PMW data  
2 dating back to 1978, allowing us to study seasonal snow climatological changes (Takala et al., 2011;  
3 Takala et al., 2017; Santi et al., 2012). These superiorities make snow depth estimation from satellite  
4 PMW remote sensing an attractive option.

5 However, there are two challenges when generating long-term snow depth data. The first challenge  
6 is choosing the most suitable algorithm. The most widely used inversion algorithms are based on  
7 empirical relationships between spaceborne satellite brightness temperature ( $T_B$ ) differences (high  
8 frequency sensitive to snow volume scattering ~37 GHz and low frequency insensitive to snow ~19 GHz)  
9 and snow depth (Chang et al., 1987; Foster et al., 1997; Derksen et al., 2005; Che et al., 2008; Kelly et  
10 al., 2003; Kelly et al., 2009; Chang et al., 2009; Jiang et al., 2014; Yang et al., 2019). However, these  
11 algorithms are always not reliable in all regions using the fitted empirical constants (Davenport et al.,  
12 2011; Derksen et al., 2010; Che et al., 2016; Takala et al., 2017; Yang et al., 2019). Subsequently, more  
13 advanced algorithms that use theoretical or semiempirical radiative transfer models were developed  
14 (Durand et al., 2006; Jiang et al., 2007; Tedesco et al., 2010; Takala et al., 2011; Picard et al., 2012;  
15 Luojus et al., 2013; Che et al., 2014; Lemmetyinen et al., 2015; Metsämäki et al., 2015; Tedesco et al.,  
16 2016; Huang et al., 2017; Larue et al., 2017; Pan et al., 2016; Pan et al., 2017; Saberi et al., 2017),  
17 however, these algorithms were computationally expensive and required complex ancillary data or prior  
18 knowledge to provide accurate predictions. These factors restrict the applications of these algorithms on  
19 a global scale. Improving the performance of PMW retrieval algorithms by means of data assimilation  
20 has also been investigated (Durand et al., 2006; Tedesco et al., 2010; Che et al., 2014; Huang et al., 2017).  
21 Currently, the most representative operational assimilation system is the European Space Agency (ESA)  
22 Global Snow Monitoring for Climate Research (GlobSnow) SWE product, which combines synoptic  
23 weather station data with satellite PMW radiometer measurements through the snow forward model  
24 (Helsinki University of Technology snow emission model, HUT) (Pulliainen et al., 1999; Pulliainen.,  
25 2006; Takala et al., 2011; Luojus et al., 2013; Metsämäki et al., 2015; Takala et al., 2017). To avoid  
26 spurious or erroneous deep snow observations, a mask is used in mountainous areas (Takala et al., 2011;  
27 Luojus et al., 2013). Moreover, the product is generated in the Northern Hemisphere ( $> 35^\circ N$ ), which  
28 excludes most parts of Qinghai-Tibetan Plateau (QTP). The algorithm may not be as feasible as empirical  
29 algorithms in terms of real-time operation because of its sophisticated procedure and diverse inputs.  
30 Currently, machine learning (ML) is being utilized in many different research areas, and its early



1 application in remote sensing fields is promising (Liang et al., 2015; Bair et al., 2018; Xiao et al., 2018;  
2 Xiao et al., 2019). ML techniques can reproduce the nonlinear effects and interactions between variables  
3 without assumptions of a functional form. The widely known ML algorithms include support vector  
4 machine (SVM), artificial neural network (ANN) and random forest (RF). Among these methods, RF is  
5 an ensemble method whereby multiple trees are grown from random subsets of predictors, producing a  
6 weighted ensemble of trees (Breiman, 2001; Liang et al., 2015; Bair et al., 2018). RF is also robust against  
7 overfitting in the presence of large datasets and increases predictive accuracies over single trees. The  
8 method has been used in classification and prediction due to its proven accuracy, stability, and ease of  
9 use (Bair et al., 2018; Belgiu et al., 2016; Rodriguez-Galiano et al., 2012; Qu et al., 2019).

10 The second challenge is how to take full advantage of the data from different sensors and rebuild a  
11 long time series dataset. On the one hand, global snow estimates from PMW measurements are among  
12 the longest satellite-derived climate records in existence, from the Scanning Multichannel Microwave  
13 Radiometer (SMMR, 1978-1987), Special Sensor Microwave/Imager (SSM/I, 1987-2008) and Special  
14 Sensor Microwave Imager/Sounder (SSM/I-S, 2006-present) to NASA's Advanced Microwave Scanning  
15 Radiometer for the Earth Observing System (AMSR-E, 2002-2011) and AMSR2 (2012-present)  
16 (Knowles et al., 2000; Armstrong et al., 1994; Kawanishi et al., 2003; Imaoka et al., 2012). The  
17 Microwave Radiation Imager (MWRI) onboard the Chinese FengYun-3 (FY-3) series of satellites (FY-  
18 3A, 2008; FY-3B, 2010-the present; FY-3C, 2013-present; FY-3D, 2017-present) was designed for broad  
19 meteorological and environmental applications (Yang et al., 2011). Subsequent satellites, FY-3E, 3F and  
20 3G, are expected to be launched in the future until 2025. However, several consecutive generations have  
21 different sensor calibration and design characteristics, which tend to result in uncertainties and  
22 inconsistencies (Armstrong et al., 1994; Derksen et al., 2003; Cavalieri et al., 2012; Meier et al., 2011;  
23 Okuyama et al., 2015). For example, the footprint size of AMSR2 has been improved compared to its  
24 predecessors, and the grid  $T_B$  is more representative for pixels ( $25 \times 25 \text{ km}^2$ ). The 10.65 GHz included  
25 in the AMSR2 and MWRI is more suitable for the estimation of deep snow cover (Derksen et al., 2008;  
26 Kelly et al., 2009; Jiang et al., 2014). This frequency has been missed since the SSM/I substituted for the  
27 SMMR and was not available until the Global Change Observation Mission (GCOM-W) AMSR-E was  
28 operational. The SSM/I(S) sensors, including SSM/I and SSM/I-S, on the U.S. Defense Meteorological  
29 Satellite Program (DMSP) satellites (F08, F11, F13, and F17) collect data at four frequencies (19, 22, 37,  
30 85 or 91 GHz) from 1987 to the present. Although there is no 10.65 GHz frequency, the satellite sensors



1 and platforms possess similar configurations. Moreover, the latest dataset was reprocessed to complete  
2 intersensor calibrations by Remote Sensing Systems Version (RSS V7), providing interconsistency of  $T_B$   
3 from the sensors (Armstrong et al., 1994). Thus, balancing the data consistency (SSM/I and SSMI/S) and  
4 the advanced PMW instruments (AMSR2 and MWRI) is still an issue. To make use of the advantages of  
5 both aspects, we propose a pixel-based method of snow depth reconstruction and real-time estimation  
6 based on the RF model, where the RF model was trained using the 10.65-89 GHz satellite observations  
7 (AMSR2) and other ancillary data. The estimated snow depth from the RF was used to develop a pixel-  
8 based algorithm using 19.35 and 37 GHz for the SSMI(S).

9 The primary objective of this study is to test the RF model feasibility in estimating snow depth,  
10 establish a pixel-based method to retrieve real-time snow depth and reconstruct historical snow depth  
11 data (~31 years, from 1987-2018). The paper is organized as follows. The data and methodology are  
12 presented in Section 2. In Section 3, the results are described, including the RF model test, RF model  
13 training, development of a pixel-based model and long-term snow depth reconstruction. The discussion  
14 is provided in Section 4, and in Section 5, we present our conclusions.

## 15 **2 Data and Methodology**

### 16 **2.1 Data**

#### 17 (1) Satellite passive microwave measurements

18 There is a relatively long time series of remotely sensed PMW measurements (from 1978-present). Table  
19 1 shows the characteristics of PMW remote sensing sensors. Among these sensors, AMSR2 has three  
20 major advantages compared with other instruments: (a)  $T_B$ s from 10.65 GHz-89 GHz are available  
21 compared to the SMMR, SSM/I and SSMI/S sensors; (b) it contains a newly added 7.3 GHz channel at  
22 the C-band compared to the previous AMSR-E; and (c) the antenna is enhanced with a smaller footprint  
23 size. Thus, the overall reliability has been improved to a certain extent. Therefore, in the first step, the  
24 RF model was trained using the AMSR2 measurements to generate the reference snow depth. The  
25 AMSR2 data are provided in the EASE-Grid projection with an equidistant latitude-longitude at a quarter  
26 degree resolution since 3 July 2012 (<http://gportal.jaxa.jp/gpr/>). To avoid the influence of wet snow on  
27 snow depth estimation, only the  $T_B$  observations from nighttime overpasses (Descending, 1:30 a.m.) were  
28 used in this paper (Chang et al., 1987; Derksen et al., 2010; Tedesco et al., 2016).



1 The SSMI(S) sensors provide  $T_B$  data at 19.35, 23.235, 37, 85.5 or 91.655 GHz from 1987-present.  
2 The data are available from the National Snow and Ice Center  
3 (<https://daacdata.apps.nsidc.org/pub/DATASETS>). Both the vertical and horizontal polarizations are  
4 measured, except for 23.235 GHz, where only the vertical polarization is measured. The satellite sensors  
5 and platforms with similar configurations can reduce system errors, which is suitable for producing a  
6 long-term consistent snow depth dataset. We used the dataset reprocessed by RSS, in which the  
7 intersensor calibrations were completed. To avoid the influence of wet snow, only cold overpass data  
8 were used. Notably, in this study, the difference between 19.35 (36.5) GHz and 18.7 (37) GHz was  
9 ignored.

#### 10 (2) In situ measurements

11 The weather station data were acquired from the National Meteorological Information Centre, China  
12 Meteorology Administration (CMA). The snow depth measurement dataset used in this paper is from  
13 689 stations throughout China (Fig. 1, left) from 2012-2018. The recorded variables include the site name,  
14 observation time, geolocation (latitude and longitude), elevation (m), near surface soil temperature  
15 (measured at a 5-cm depth, °C), and snow depth (cm). Notably, because of the harsh climate and complex  
16 terrain, meteorological stations are few in the QTP, especially in the western part.

17 Quality control was conducted prior to using the data for developing the retrieval algorithm. The first  
18 step was to select the records where the near surface soil temperature was lower than 0 °C. The second  
19 step was to remove the sites if the areal fraction of the open water exceeded 30 % within a satellite pixel.  
20 Finally, only ground-measured snow depths greater than 3 cm were used because the microwave response  
21 to thinner snow cover at 37 GHz is basically negligible (Derksen et al., 2010; Tedesco et al., 2016). A  
22 small number of points with extremely high snow depth values (greater than 70 cm) were also removed.  
23 The snow depth distribution in the filtered subset is from 3-70 cm.

24 In addition, the field campaign supported by the Chinese snow survey (CSS) project was conducted  
25 from January-March in 2018 to measure the snow depth transects in two satellite pixels in Xinjiang and  
26 Northeast China (Wang et al., 2018). Figure 1 shows the two field sampling pixels in Xinjiang and  
27 Northeast China. Table 2 shows the details of the snow field sampling work, including longitude, latitude,  
28 altitude (m) and land cover types. The lack of canopy cover makes it an ideal study area for PMW remote  
29 sensing. There are 26 and 21 sampling measurements within a coarse 25 km pixel in Xinjiang and  
30 Northeast China, respectively. There were four days of snow depth transect measurements on January



1 21, 23, February 1 and March 9, 2018. For field sampling, measurements within each grid are averaged  
2 to represent the ground truth snow depth.

### 3 (3) Land cover fraction

4 A 1-km land use/land cover (LULC) map derived from the 30-m Thematic Mapper (TM) imagery  
5 classification was provided by the Data Center for Resources and Environmental Sciences, Chinese  
6 Academy of Sciences (<http://www.resdc.cn/>). Because the 1-km LULC map was derived from 30-m TM  
7 imagery, the map can be recalculated as the areal percentages of each land cover type in the 25-km grid  
8 cells. In this study, the fractions of grass, barren, farm, forest, and shrub were calculated as inputs of the  
9 RF model. The dataset is not described here; see Jiang et al. (2014) for more details. To avoid the  
10 influence of water bodies and construction, the record was used only if the total fraction, including grass,  
11 barren, farm, forest, and shrub, was greater than 60 %.

## 12 2.2 Methodology

### 13 (1) Stability test of RF

14 RF is an ensemble algorithm that was developed by Breiman in 2001. RF runs by constructing many  
15 single decision trees to improve performance, which is much more efficient than traditional ML  
16 techniques. The RF algorithm generally only requires two user-defined parameters, the number of trees  
17 in the ensemble, and the number of random variables at each node. A particular advantage of RF is that  
18 because of the presence of multiple trees, the individual trees need not be pruned, avoiding overfitting  
19 (Breiman, 2001). In this paper, the RF method is trained to retrieve the reference snow depth dataset,  
20 which is necessary to build the pixel-based model.

21 In general, the quality of the reference snow depth is determined by the RF model performance. In  
22 this study, the number of variables selected at each node (split) is set to 4 (usually the square root of the  
23 number of input variables) based on the number of input variables (Gislason et al., 2006; Belgiu et al.,  
24 2016). The number of trees is set to 500 according to the out-of-bag (OOB) test because the errors are  
25 stable when the number of decision trees is adequate. This finding agrees with previous studies  
26 suggesting that a tree number of approximately 500 is generally sufficient (Belgiu et al., 2016; Cánovas-  
27 García et al., 2015; Cánovas-García et al., 2017; Tsai et al., 2019). However, how many samples should  
28 be inputted to the RF model? Specifically, is the performance of the RF model related to the training



1 samples? Thus, the RF's performance is tested in terms of different training datasets. The flowchart of  
2 the test process is shown in Fig. 2.

3 There are 80000 pairs of samples from 1987-2004 (including PWM  $T_B$  from SSM/I, land cover  
4 fraction and in situ snow depth). Notably, the SSM/I  $T_B$  pairs here are only used to test the number of  
5 samples required, not the ultimate training data of the RF model. During this process, the number of  
6 samples selected randomly is from 5000 to 80000 (step, 5000). A unified dataset from 2005-2006 is used  
7 to evaluate the performance of the RF model. We consider three evaluating indicators (the root mean  
8 square error (RMSE), bias and correlation coefficient) to illustrate the stability of the RF model.

9 (2) RF model training, reference snow depth and the pixel-based model

10 The main processing steps are described in detail in Fig. 3. To build the RF model, as shown in Table 3,  
11 the training dataset is composed of fifteen predictors including land cover fraction (5), latitude (1),  
12 longitude (1), AMSR2  $T_B$  (8) and one target - station snow depth (1) from 2014 to 2015 (45000 samples).  
13 The data were used to validate the trained model in the period from 2012 to 2013. The PMW  
14 measurements contain dual-polarized (H & V)  $T_B$ s in four channels: 10.65 GHz, 18.7 GHz, 36.5 GHz  
15 and 89 GHz. All available channels on the AMSR2 are listed in Table 1. Specifically, the 6.925 GHz and  
16 7.3 GHz channels are contaminated by radio frequency interference (RFI) and are not sensitive to  
17 snowpack (Kelly et al., 2009; Rodríguez-Fernández et al., 2015). The 23.8 GHz channel is sensitive to  
18 water vapor and not surface scattering, which introduces uncertainty to the estimation process. Typically,  
19 the lower frequency (18.7 GHz) is used to provide a background  $T_B$  against which the higher frequency  
20 (36.5 GHz) scattering-sensitive channels are used to retrieve snow depth. However, the possibility that  
21 deep snow can scatter 18.7 GHz radiation suggests that a lower frequency (10.65 GHz) is more suitable  
22 to provide background information (Kelly et al., 2009; Derksen et al., 2008; Tedesco et al., 2016). The  
23 89 GHz channel was added because of its penetrability of shallow snow. For shallow snow or fresh snow,  
24 it is probably transparent for 36.5 GHz. Thus, the use of 89 GHz channels can greatly improve depth  
25 retrieval for barren land (Jiang et al., 2014). The mixed-pixel problem is the dominant limitation on snow  
26 depth estimation accuracy (Derksen et al., 2005; Kelly et al., 2009; Jiang et al., 2014; Roy et al., 2014;  
27 Cai et al., 2017; Li et al., 2017; Li et al., 2019). Satellite  $T_B$  usually represents several land cover types  
28 due to coarse footprints (tens of km). Thus, we added the main land cover fraction as part of the training  
29 dataset. Some previous studies have shown that latitude and longitude contribute to improving RF model  
30 performance and present the spatial distribution of snow depth (Bair et al., 2018; Qu et al., 2019).





1 After the RF model was trained, it was validated with the AMSR2  $T_B$  and station snow depth of 2012-  
2 2013. Then, the trained RF model was used to generate a relatively accurate snow depth dataset (hereafter  
3 referred to as the reference dataset) with AMSR2 observations from 2012 to 2018 (Fig. 3, step 1). We  
4 hypothesize that the snow depth estimates with the RF model are the most accurate ground truth available.  
5 Then, the reference snow depth was used to establish a pixel-based algorithm using the  $T_B$  gradient (19.35  
6 GHz-37 GHz):

$$7 \quad SD = Slope \times (T_{B19.35H} - T_{B37H}) + Intercept \quad (1)$$

8 where the *Slope* and *Intercept* are dynamic coefficients for each grid.  $T_{B19.35H}$  and  $T_{B37H}$  are PMW  
9 brightness temperatures in Kelvin (K) at horizontal polarization. SD is snow depth in centimeters from  
10 the reference data. The development of a pixel-based retrieval method makes it possible to estimate real-  
11 time snow depth without relying on the use of multiple sources of information.

12 The performance of the pixel-based method was also compared with the static linear-fitting algorithm  
13 developed by fitting 19.35 and 37 GHz with the snow depth measurements with a constant empirical  
14 coefficient over China (Fig. 3, step 2). The linear-fitting method is the modified Chang equation, which  
15 was developed based on Chinese weather station observations and SSM/I  $T_B$  for China (Che et al., 2008).  
16 The equation is as follows:

$$17 \quad SD = 0.66 \times (T_{B19.35H} - T_{B37H}) \quad (2)$$

18 where the  $T_{B19.35H}$  and  $T_{B37H}$  are brightness temperatures for 19.35 GHz and 37 GHz at horizontal  
19 polarization, respectively and 0.66 is the static fitting coefficient.

### 20 (3) The reconstructed snow depth product and validation

21 The reconstructed snow depth dataset from 1987 to 2018 with the pixel-based method was evaluated by  
22 the in situ measurements from the weather stations (2017-2018) and the field snow transects from the  
23 CSS (January to March 2018). Then, the spatiotemporal distribution of snow depth was analyzed (Fig. 3,  
24 step 3). To ensure the possible dry snow cover, the reconstruction periods are the main snow winter  
25 seasons (January, February, March, November, and December).

## 26 3 Results

### 27 3.1 RF stability test



1 Although RF has many advantages over other ML techniques, the performance is related to the number  
2 of training samples. Moreover, the quality of the reference snow depth is determined by the performance  
3 of the RF model. To conduct a complete test with enough samples, 80000 pairs of records from 1987 to  
4 2004 were used to test the required size of the training samples. The results are shown in Fig. 4 after  
5 several test runs. Figure 4a represents the RMSEs range from 5.1 cm to 5.4 cm with increasing samples.  
6 Figure 4b shows slight fluctuations of bias between -0.2 and 0.2 cm. Figure 4c shows that the correlation  
7 coefficient is as high as 0.79 and seems to be stable when the samples are up to 50000. In any case, the  
8 figure shows that the RF model performs robustly in terms of the training sample subset. In other words,  
9 the number of training samples has less influence on the prediction accuracy because of the sufficient  
10 number (500) of single decision trees (Belgiu et al., 2016; Cánovas-García et al., 2015; Cánovas-García  
11 et al., 2017; Bair et al., 2018). The test is very helpful for us to determine the number of training samples  
12 because of limited training samples from AMSR2.

### 13 3.2 RF model training and validation

14 To obtain a spatially continuous and accurate reference snow depth dataset, the RF model was used to  
15 find the nonlinear relationship linking the input data to the target. The input data are composed of the  
16 AMSR2  $T_B$ , land cover fraction and geolocation (Table 3). The target dataset used to train the RF is from  
17 weather station observations in 2014 and 2015. The performance of the trained RF model was evaluated  
18 by the weather station snow depth in 2012 and 2013. Figure 5a shows that the RMSE is 4.5 cm. The  
19 determination coefficient is as high as 0.77. Figure 5b shows the spatial distribution of RMSE. The  
20 pattern of the high RMSE is consistent with the mountains (Xinjiang: Altai Mountains and Tianshan  
21 Mountains; Northeast China: Changbai Mountains and Xiao Hinggan Mountains), which means that the  
22 accuracy is low in that location. Additionally, the large uncertainties in snow depth retrieval are  
23 associated with forest cover in Northeast China, which agrees with the studies by (Cai et al., 2017; Li et  
24 al., 2017; Roy et al., 2014; Liu et al., 2018). The RMSE in the QTP and South China is also large due to  
25 patchy, shallow and wet snow (Dai et al., 2017, 2018; Yang et al., 2015). Figure 5c shows that it tends  
26 to overestimate snow depth over shallow snow areas, especially in the QTP and South China. In these  
27 areas, weather stations are sparsely distributed, and snowfall is ephemeral. The snow cover is as thin as  
28 1~5 cm, which challenges the ability of PMW remote sensing. Figure 5d shows the spatial distribution  
29 of relative errors (RMSE is divided by mean snow depth). The error in the shallow snow cover is higher



1 than that in the thick snow areas. This pattern is caused by the low mean snow depth. Similarly,  
2 occasionally, a high RMSE does not mean a poor performance because the relative error is less than 20 %,   
3 for example, for the sites in northern Xinjiang and the Heilongjiang Province.

4 Long-term snow depth datasets retrieved from the RF model and linear-fitting model are compared  
5 with the station observations in three regions of China (Fig. 6). There are sixteen pixels, three pixels and  
6 one pixel in Northeast China, Xinjiang and the QTP, respectively. The land cover types are mainly  
7 farmland in Northeast China, grassland in Xinjiang and grassland in the QTP. In situ measurements of  
8 mean snow depth are obtained for the sites within each region. The results show that the linear-fitting  
9 method performance is unstable. It tends to underestimate snow depth at the beginning of the snow season  
10 but overestimate the snow depth in the late winter. This is because the grain size and density of fresh  
11 snow are very small, so the scattering effect is nearly negligible. Along with the seasonal evolution, the  
12 snow particle grows (~2 mm), and the snowpack becomes denser (200~400 kg m<sup>-3</sup>), which causes  
13 stronger scattering effects. In situ measurements show that the snow cover is shallow in the QTP, even  
14 less than 5 cm, which results in patchy snow cover (Dai et al., 2017). However, the snow depth was  
15 overestimated, which may be due to the following reasons. First, the data with a depth thinner than 3 cm  
16 were excluded from the training dataset. Second, a distinct meteorological characteristic of the QTP is  
17 the large diurnal temperature range, which causes snow to undergo frequent freeze-thaw cycles and leads  
18 to rapid snow grain growth and consequently a high T<sub>b</sub> difference (Durand et al., 2008; Yang et al., 2015;  
19 Dai et al., 2017). Third, frozen soil is also a factor that reduces the accuracy of estimates in the QTP.  
20 Both snow and frozen ground are volume scattering materials, and they have similar microwave radiation  
21 characteristics, making them difficult to distinguish (Chang et al., 1987; Grody and Basist., 1996).

22 Figure 7 shows the spatial distribution of the monthly average snow depth (winter season, 2016). The  
23 left figure is the station observation; the middle figure is the RF estimation; and the right figure is the  
24 linear-fitting model estimation. The five rows present mean snow depths in January, February, March,  
25 November and December. The patterns between the RF estimations and station measurements are similar,  
26 especially in Northeast China and Xinjiang. In November, December and January, serious  
27 underestimation occurs for the linear-fitting model. This is because fresh snow has little scattering effect,  
28 and the forest canopy attenuates the ground signals (Che et al., 2016; Li et al., 2019). Moreover,  
29 overestimation occurs in February and March due to strong scattering caused by snow microphysical  
30 properties, such as snow grain size and density (Che et al., 2016; Dai et al., 2017; Yang et al., 2019). In



1 November and December, sites recording snow cover are very sparsely distributed in Tibet, Qinghai and  
2 western Inner Mongolia. Thus, it is difficult to assess the performances of the two methods. Although  
3 the station sites show snow cover in southern China, the snowpack identification method does not classify  
4 snow as snow (Li et al., 2007; Liu et al., 2018). In February, there are many site records in central China,  
5 including Gansu, Ningxia and Shanxi. The comparison demonstrates that the RF model tends to  
6 overestimate snow depth in these areas. This is related to the sparse sites and ephemeral snowfall events,  
7 which result in poor representativeness. The snow cover is as thin as 1~5 cm in these areas, which makes  
8 PMW remote sensing weak for estimating snow depth. Another reason is that the sample record is  
9 removed if the in situ snow depth is below 3 cm. Thus, training samples of the RF model also give  
10 estimates higher than 3 cm. Additionally, snow depth estimation in the mountains remains a challenge  
11 (Lettenmaier et al., 2015; Dozier et al., 2016). The RF model and linear-fitting method have sharply  
12 different performances in the Himalayan range. Numerous studies have been conducted on the snow  
13 cover over the QTP and have indicated that the snow cover frequency in the Himalayas is higher than  
14 elsewhere, ranging from 80 % to 100 % during the winter seasons (Basang et al., 2017; Hao et al., 2018).  
15 Additionally, Dai et al. (2018) showed that deep snow (greater than 20 cm) was mainly distributed in the  
16 Himalaya, Pamir, and Southeastern Mountains. The spatial distribution of snow depth in spring (March,  
17 April and May) and winter (December, January and February) showed that the annual mean snow depth  
18 is greater than 20 cm in the Himalayas (Dai et al., 2018). The pattern based on reference Dai et al. (2018)  
19 is similar to the results of the RF model in this study. Obviously, the linear-fitting method does not  
20 capture the deep snow cover in the Himalayas.

### 21 **3.3 Pixel-based model and validation**

22 Based on the reference snow depth retrieved with the RF model (in Sect. 3.2) and  $T_B$  gradient between  
23 19.35 GHz and 37 GHz at horizontal polarization (Eq. (1)), the *Slope* and *Intercept* of the pixel-based  
24 model are determined in Fig. 8a and 8b. The *Slope* and *Intercept* are set to 0 when there are no samples  
25 for some pixels where it is impossible for snow to fall. The interpolation method (3×3 sliding window,  
26 average value) is used to determine the *Slope* and *Intercept* in which the number of samples is between  
27 3 and 10. The *Slope* is high in Northeast China and Northern Xinjiang. It is also high in the Himalayas  
28 and the Pamir, where the snow cover is thick. The *Intercept* is low in unstable snow-covered areas,  
29 including Inner Mongolia and central and South China. The RMSE between the reference data and



1 estimates is shown in Fig. 8c. The mean RMSE is approximately 3.2 cm. In most areas, the RMSE is less  
2 than 5 cm. However, the RMSE is very high in South China, where snowfall is highly unlikely to occur.  
3 From 2012 to 2018, there are no more than 3 snowfall events in South China. Thus, the *Slope* and  
4 *Intercept* are directly set to 0.66 and 0, respectively. In northern Xinjiang and Northeast China, a high  
5 RMSE occurs over the Tianshan and Altai Mountains, Changbai Mountains and Xiao Hinggan  
6 Mountains. These areas not only have varied topography but are also covered with forest or shrub. The  
7 correlation between the reference snow depth and estimated snow depth with the pixel-based model is  
8 shown in Fig. 8d. Obviously, the pattern of correlation is in accordance with snow cover types. Stable  
9 snow cover areas present high correlations (Xinjiang and Northeast China) due to dry and nearly full  
10 coverage snow cover (Yang et al., 2019). The correlation is very low and even negative in most areas of  
11 South China, which are shown in white in Fig. 8d.

12 In this study, a long-term snow depth dataset (1987 to 2018) was reconstructed with a pixel-based  
13 model in Sect. 3.2. To evaluate the snow depth product, we use ground-based truth snow depth  
14 measurements from two sources: weather station and field sampling. Weather station snow depth is  
15 retrieved during the winter season from 2017 to 2018, independent of training samples of the pixel-based  
16 model. Field measurements are taken from CSS, providing records of dense snow depth sampling within  
17 a coarse pixel across Xinjiang and Northeast China in 2018 (Fig. 1). As shown in Fig. 9a, there is good  
18 agreement between the snow depth estimated with the pixel-based model and the measured snow depth.  
19 The RMSE is 2.0 cm, and the determination coefficient reaches as high as 0.91, which is much better  
20 than the linear-fitting method coefficients of 4.7 cm and 0.52. The station data validation is shown in Fig.  
21 9b. The error bar shows that the linear-fitting method tends to seriously underestimate (bias is -2.6 cm)  
22 when the snow depth is over 10 cm. The pixel-based model overestimates the shallow snow cover (less  
23 than 5 cm), but the overall accuracy is higher than the linear-fitting method.

24 The time series of snow depth retrieved from the pixel-based model and linear-fitting method are  
25 compared with the station observations in three regions of China (Fig. 10). The results show that the  
26 pixel-based model performs better than the linear-fitting method in Northeast China and Xinjiang. The  
27 linear-fitting method tends to underestimate snow depth at the beginning of the snow season (November  
28 and December) but overestimates the snow depth in the late winter (February and March). However, the  
29 snow depth was seriously overestimated for the pixel-based method in the QTP. The reasons were shown  
30 in Sect. 3.2. Most parts of the QTP are covered with shallow snow. Deep snow is distributed in the



1 Himalaya, Pamir, and Southeastern mountainous areas. However, there are no in situ observations in  
2 these areas due to complex terrain and atmospheric conditions, resulting in validation failure.

### 3 **3.4 Spatial-temporal analysis of the reconstructed snow depth**

4 The spatial-temporal distribution of snow depth over China is analyzed based on a reconstructed snow  
5 dataset (1987-2018). The time series of snow depth in different regions over China is shown in Fig. 11.  
6 The black, green, blue and magenta lines represent daily mean or maximum snow depth in China,  
7 Northeast China, Xinjiang and the QTP, respectively. Figure 11a shows that the daily mean snow depth  
8 in Northeast China is larger than that in Xinjiang and the QTP for most years. The mean snow depth in  
9 the QTP is the smallest (< 12 cm). Please note that the mean snow depth over the QTP is the highest in  
10 1998, which aggravated major flooding in the area of the middle and lower reaches of the Yangtze River  
11 (Dorji et al., 2018). Figure 11b shows the time series of daily maximum snow depth. The maximum snow  
12 depth is most likely to occur in Xinjiang and the QTP, although the mean snow depth is large in Northeast  
13 China. The maximum is usually distributed in the QTP Himalayas during these years, such as 1996, 1998,  
14 1999, 2009, 2010 and 2015.

15 To show the monthly snow depth difference for every year, the time series of the yearly snow depth  
16 for winter seasons is shown in Fig. 12. Because there are only two months (November and December)  
17 and three months (January, February, March) of snow depth records in 1987 and 2018, respectively, the  
18 period is from 1988 to 2017. The results show that the mean snow depths in February and March are  
19 higher than the yearly average snow depth. The mean in November is smallest and below 10 cm during  
20 the winter seasons. The mean snow depth in January is basically on behalf of the annual mean snow  
21 depth but for individual years, such as 1988 and 1994. This is highly important for predicting snow depth  
22 in hydrologic studies.

23 On the spatial scale, the time series of snow depth in different subregions is analyzed. Figure 13  
24 shows that the annual mean snow depth in Xinjiang and Northeast China is above average over China.  
25 The mean in Northeast China is the largest among the three subregions. However, the maximum snow  
26 depth has a tendency not to occur in Northeast China. The yearly mean snow depth in the QTP is the  
27 smallest among the three subregions. However, the maximum sometimes occurs in the QTP (Fig. 11).  
28 Thus, the spatial pattern of snow depth in the QTP exhibits great heterogeneity (Fig. 7).



## 1 **4 Discussion**

### 2 **4.1 Spatial correlation and bias between the RF model and pixel-based method**

3 To obtain further insight into the ability of the pixel-based method to capture the temporal and spatial  
4 variability in snow depth, it is essential to compare the pixel-based retrievals with respect to the reference  
5 snow depth dataset retrieved with the RF model. Figure 14a shows a scatter plot of snow depth retrieved  
6 by the RF model vs. the pixel-based method. The coefficient of determination is very high ( $R^2=0.83$ ).  
7 The pixel-based product displays a very strong correlation with the reference snow depth dataset. A  
8 histogram of the bias (RF minus pixel-based method) distribution is shown in Fig. 14b and suggests that  
9 the mean bias is very small (0.47 cm), and most biases are between -2 cm and 2 cm. Figure 14c shows  
10 the time series of the spatial correlation ( $R$ ) of retrieval RF with respect to the pixel-based method. The  
11 mean value of  $R$  is 0.91, which is a strong correlation between RF and the pixel-based method. The time  
12 series of correlation show a seasonal oscillation, with slightly lower values for months during late autumn  
13 (November) and early spring (March). This is because the snow cover is patchy and shallow in November,  
14 challenging the relationship between satellite  $T_B$  and snow depth (Dai et al., 2017; Yang et al., 2019). In  
15 addition, snowfall is also ephemeral and occurs in the mountains. The results may be affected by  
16 variations in the number of samples and the station representativeness. Thus, the reference snow depth  
17 retrieved with RF may still be inaccurate. Another limiting factor in estimating snow depth from PMW  
18 data is the presence of liquid water because of the relatively high air temperature in these months,  
19 resulting in higher absorption and poor penetration depth. Consequently, the satellite observation is  
20 mainly associated with the emissions from the wet surface of the snowpack. Therefore, in wet snow  
21 conditions, snow depth retrieval is not possible (Chang et al., 1987; Foster et al., 1997; Derksen et al.,  
22 2010; Tedesco et al., 2016). The time series of mean biases in Fig. 14c shows that bias is within  $\pm 1$  cm.  
23 In any case, the pixel-based method, which uses only satellite data as input, shows the robustness as its  
24 performances are comparable to the performances of RF over the training period.

### 25 **4.2 Disadvantages and potential errors of the reconstructed snow depth**

26 There are no available in situ measurements over all of China to ensure that the training dataset is  
27 statistically significant to perform spatial inversions once the RF is trained. Thus, the accuracy of the  
28 pixel-based algorithm is uncertain in the mountains or high-altitude areas where few stations are  
29 distributed. In addition, the problem of training the RF with in situ measurements is that the



1 measurements are point measurements while the satellite grids have a spatial resolution of  $25 \times 25$  km<sup>2</sup>.  
2 Moreover, only the 19.35 and 37 GHz are H-pol. T<sub>B</sub>s values were used to yield the long-term  
3 reconstructed snow depth through the pixel-based method. Comparing Fig. 5 and Fig. 9b, the diminished  
4 underestimation of snow depth by the RF model for the 20-60 cm thick snow appeared again in the pixel-  
5 based regression model. Therefore, some snow depth underestimation is still possible in the reconstructed  
6 snow depth dataset.

#### 7 **4.3 Variable Importance in RF Model**

8 RF can examine the predictor importance as an increased mean squared error which is calculated by  
9 summing changes using every split for a predictor, then dividing by the total number of splits (Breiman,  
10 2001; Bair et al., 2018). The larger this value, the greater the importance of the variable. Figure 15 shows  
11 the importance of all the input independent variables in the RF model. The results indicate that T<sub>B</sub> at 36.5  
12 GHz is by far the most important predictor, with values of 44 % and 43 % for horizontal and vertical  
13 polarizations, respectively, showing that the PMW snow depth retrievals have significant predictive  
14 power for dry snow cover. The third most important predictor is longitude, followed by latitude, which  
15 makes the RF model more dependent on station data.

16 Figure 16 shows the spatial patterns of the reconstructed snow depth over China for 1992-2017 at  
17 intervals of five years. The deep snow cover is mainly distributed in Xinjiang, Northeast China and the  
18 QTP (Himalayas). Moreover, the distribution of snow depth is affected by topography (the digital  
19 elevation model, DEM). For example, the elevations of the west and south QTP are higher than that of  
20 the east QTP, so that snow cover is relatively thick there (Figure 16). This phenomenon could be ascribed  
21 to two reasons: the sparsity of the sites and the significant geolocation (latitude and longitude). Figure 1  
22 shows that the stations are sparsely and unevenly distributed in the QTP. Moreover, since most of the  
23 stations are located in inhabited valleys, the representativeness of these in situ data is questionable  
24 (Orsolini et al., 2019). Another reason is that inputs of the RF model include longitude and latitude,  
25 which should contribute to the present spatial patterns of snow depth according to previous studies  
26 (Belgiu et al., 2016; Qu et al., 2019, Xiao et al., 2018, Wang et al., 2019). In fact, the longitude and  
27 latitude reflect the DEM information, which greatly affects the Plateau's vegetation, precipitation and  
28 snowfall (Qu et al., 2019, Wang et al., 2019).

#### 29 **4.4 Influence of land cover types on product accuracy**





1 The evaluation of the pixel-based method performance with station observations from 2017 to 2018  
2 revealed that the snow depth product accuracy varies significantly between land cover classes (Table 4).  
3 The grids are viewed as pure pixels where the land cover fraction is greater than 85 % (Jiang et al., 2014).  
4 Densely forested regions tend to yield a higher RMSE (6.2 cm) and lower determination coefficient (0.43)  
5 when compared to grassland and farmland (Table 4). RMSEs in open areas, such as grassland (5.5 cm),  
6 farmland (4.2 cm) and barren (4.6 cm), are low due to no canopy influence on the satellite observations  
7 (Derksen et al., 2005; Cai et al., 2017; Che et al., 2016; Li et al., 2017). The determination coefficient for  
8 grassland is as high as 0.74, which shows that the snow cover is homogeneous and that the station snow  
9 depth is representative of satellite pixels (Yang et al., 2019). The determination coefficient of barren is  
10 0.35 because of shallow, patchy snow cover and poor station representativeness (Dai et al., 2018; Yang  
11 et al., 2019). This study demonstrates that the underlying surface condition influences the snow depth  
12 estimation with a pixel-based approach. One of the future developments to improve the product accuracy  
13 will be training the RF model separately for each land cover class.

#### 14 **4.5 RF model trained by snow emission model simulations**

15 In this study, the RF model's performance determines the accuracy of the reconstructed snow depth. The  
16 input variable describing the snow cover is only snow depth. The more prior information there is on snow  
17 cover, the better the performance of the RF model will be. To determine the ability of the RF model, the  
18 microwave emission model of layered snowpack (MEMLS) is applied to simulate the  $T_B$  with varying  
19 snow parameters (Mätzler et al., 1999; Löwe et al., 2015; Pan et al., 2015). Table 5 shows the ranges of  
20 variable parameters and constants. The snowpack is set as one layer. Then, 10000 combinations of  
21 parameters are randomly chosen in the range by the computer, and these combinations are inputted to  
22 MEMLS to simulate the multifrequency brightness temperatures (10, 18.7, 37 and 89 GHz at H and V  
23 polarizations). The training dataset of the RF model is composed of  $T_B$ , snow depth, snow density and  
24 correlation length. Finally, two-thirds of the samples are inputted to the RF to train the model. One-third  
25 of the samples are used to test the performance in estimating snow depth.

26 To illustrate that more snow cover information can improve the accuracy of the RF model, two sets  
27 of samples are inputted to the RF model. One set includes the 10-89 GHz observations, snow depth, snow  
28 density and grain correlation length. Another set consists of 10-89 GHz brightness temperatures and  
29 snow depth only. The measured snow depth is the initial input of the MEMLS. The estimated snow depth



1 is retrieved with the RF model. Figure 17a shows that more snow parameter inputs (snow density and  
2 snow grain size) describing snow cover characteristics can improve the accuracy of snow depth  
3 estimation. Otherwise, the scatter plots are dispersed, namely, there is a large RMSE between the truth  
4 measurement and estimated snow depth (Figure 17b). Thus, the snow parameters retrieved with snow  
5 models and measured in the field work are significant for improving the RF model. How to combine the  
6 snow forward model with the ML method will be the focus of future work.

## 7 **5 Conclusions**

8 In this study, a novel approach called a pixel-based algorithm based on the RF model was proposed to  
9 reconstruct snow depth using legacy PMW remote sensing satellite data. The RF model was trained using  
10 AMSR2  $T_B$  and other auxiliary data. The validation showed that the RF model performs well in snow  
11 depth estimations. The RMSE is 4.5 cm. The determination coefficient was as high as 0.77. Then, a pixel-  
12 based model was built based on the reference snow depth that was retrieved with the RF model. The aim  
13 was to reconstruct the long-term snow depth datasets from 1987 to 2018. Validation results with field  
14 sampling data (weather station observations) show that the RMSE was 2.0 cm (5.1 cm), much better than  
15 the linear-fitting method value of 4.7 cm (8.4 cm). Finally, a spatial-temporal analysis based on a long-  
16 term snow depth dataset was conducted. On the spatial scale, daily maximum snow depth tended to occur  
17 in Xinjiang and the QTP, while the mean snow depth in Northeast China was the highest. On a temporal  
18 scale, the annual mean snow depth varied in February and March, and snow cover was the deepest among  
19 winter seasons. Interestingly, the mean snow depth in January was basically on behalf of the yearly mean  
20 snow depth, which is significant for predicting snow depth in hydrologic studies. In conclusion, a  
21 spatiotemporally continuous snow depth product with a 31-year time series over China was obtained  
22 from the pixel-based method. As discussed in Sect. 4, our reconstructed snow depth estimates are not  
23 perfect. However, the reconstructed long-term product maintains high accuracy relative to others. In  
24 addition to the historical data reconstruction, another merit of the presented approach is the ability to  
25 provide real-time snow depth from satellite-based measurements, while the RF model that operates on a  
26 daily basis is difficult and relies on the use of multiple sources of auxiliary data. We also realize that  
27 efforts should still be made to solve the underestimation of deep snow cover and overestimation of  
28 shallow snow cover areas. On the one hand, more prior knowledge of snow cover, such as snow cover



1 fraction, snow density, and snow grain size, is necessary to improve the RF model by means of the snow  
2 forward model. In terms of the pixel-based method, two different  $T_B$  differences ( $T_{B37GHz}-T_{B89GHz}$  and  
3  $T_{B19GHz}-T_{B37GHz}$ ) will be used to account for shallow and deep snow. On the other hand, a snow depletion  
4 curve based on the relationship between snow depth and snow cover fraction will be used to improve the  
5 snow depth retrievals in the QTP.

6  
7 *Author contributions.* L. Jiang conceived and designed the study; J. Yang produced the first draft of the  
8 manuscript, which was subsequently edited by L. Jiang, K. Luoju, J. Pan and J. Lemmetyinen; and M.  
9 Takala, S. Wu, J. Pan and J. Yang contributed to the analytical tools and methods.

10

11 *Competing interests.* The authors declare that they have no conflicts of interest.

12

13 *Acknowledgments.* This study was supported by the Science and Technology Basic Resources  
14 Investigation Program of China (2017FY100502) and the National Natural Science Foundation of China  
15 (41671334). The authors would like to thank the China Meteorological Administration, National  
16 Geomatics Center of China, National Snow and Ice Data Center and NASA's Earth Observing System  
17 Data and Information System for providing the meteorological station measurements, land cover  
18 products and satellite datasets.

19 *Data availability.* Satellite passive microwave measurements are available for download from  
20 <http://gportal.jaxa.jp/gpr/> and <https://nsidc.org/>. The in-situ measurements provided by China  
21 Meteorology Administration (CMA) and Chinese snow survey (CSS) project are not available to the  
22 public due to legal constraints on the data's availability. The land use/land cover (LULC) map is provided  
23 by the Data Center for Resources and Environmental Sciences, Chinese Academy of Sciences  
24 (<http://www.resdc.cn/>). The Shuttle Radar Topography Mission (SRTM) version 004 digital elevation  
25 model (DEM) data with 90m resolution was obtained from <http://srtm.csi.cgiar.org>.

## 26 **References**

27 Armstrong, R., Knowles, K., Brodzik, M., and Hardman, M.: DMSP SSM/I-SSMIS Pathfinder Daily  
28 EASE-Grid Brightness Temperatures, Version 2. Boulder, Colorado USA. NASA National Snow and  
29 Ice Data Center Distributed Active Archive Center, 10.5067/3EX2U1DV3434, 1994.

30 Armstrong, R.; Knowles, K.; Brodzik, M.; and Hardman, M.: DMSP SSM/I-SSMIS Pathfinder Daily  
31 EASE-Grid Brightness Temperatures, Version 2; NASA National Snow Ice Data Center Distributed  
32 Active Archive Center: Boulder, CO, USA, Available online: [http://nsidc.org/data/docs/daac/nsidc0032-ssmi\\_ease\\_tbs.gd.html](http://nsidc.org/data/docs/daac/nsidc0032-ssmi_ease_tbs.gd.html),1994; Updated 2016;

34 Bair, E. H., Abreu Calfa, A., Rittger, K., and Dozier, J.: Using machine learning for real-time estimates  
35 of snow water equivalent in the watersheds of Afghanistan, The Cryosphere, 12, 1579-1594, 10.5194/tc-  
36 12-1579-2018, 2018.

37 Basang, D., Barthel, K., Olseth, JA.: Satellite and Ground Observations of Snow Cover in Tibet during  
38 2001–2015, Remote Sensing, 9,1201,10.3390/rs9111201, 2017.



- 1 Belgiu, M., and Lucian, D.: Random forest in remote sensing: A review of applications and future  
2 directions, *ISPRS Journal of Photogrammetry and Remote Sensing*, 114, 24–31.  
3 10.1016/j.isprsjprs.2016.01.011, 2016.
- 4 Bradley, R., Clague, J., Vuille, M., Buytaert, W., Cayan, D., and Greenwood, G.: Toward mountains  
5 without permanent snow and ice, *Earth's Future*, 5, 418–435, 10.1002/2016EF000514, 2017.
- 6 Breiman, L. Random forests. *Mach. Learn.* 2001, 45, 5–32, <https://doi.org/10.1023/A:1010933404324>,  
7 2001.
- 8 Chang, A., Foster J., Hall D.: Nimbus-7 derived global snow cover parameters, *Annals of Glaciology*, 9,  
9 39–44, 10.1017/S0260305500000355, 1987.
- 10 Che, T., Dai, L., Zheng, X., Li, X., Zhao, K.: Estimation of snow depth from passive microwave  
11 brightness temperature data in forest regions of northeast China, *Remote Sensing of Environment*, 183,  
12 334–349, 10.1016/j.rse.2016.06.005, 2016.
- 13 Che, T., Li, X., Jin, R., Armstrong, R., and Zhang, T.: Snow depth derived from passive microwave  
14 remote-sensing data in China, *Annals of Glaciology*, 49,145–154,10.3189/172756408787814690, 2008.
- 15 Che, T., Li, X., Jin, R., and Huang, C.: Assimilating passive microwave remote sensing data into a land  
16 surface model to improve the estimation of snow depth, *Remote Sensing of Environment*, 143, 54–  
17 63,10.1016/j.rse.2013.12.009, 2014.
- 18 Cai, S., Li, D., Durand, M., and Margulis, S.: Examination of the impacts of vegetation on the correlation  
19 between snow water equivalent and passive microwave brightness temperature, *Remote Sensing of*  
20 *Environment*, 193, 244–256, 10.1016/j.rse.2017.03.006, 2017.
- 21 Canovas-Garcia, F., Alonso-Sarria, F.: Optimal combination of classification algorithms and feature  
22 ranking methods for object-based classification of submeter resolution Z/1-Imaging DMC imagery,  
23 *Remote Sensing*, 7, 4651–4677, 10.3390/rs70404651, 2015.
- 24 Canovas-Garcia, F., Alonso-Sarria, F., Gomariz-Castillo, F., and Onate-Valdivieso, F.: Modification of  
25 the random forest algorithm to avoid statistical dependence problems when classifying remote sensing  
26 imagery, *Comput. Geosci*, 103, 1–11, 10.1016/j.cageo.2017.02.012, 2017.
- 27 Cavalieri, D., Parkinson, C., DiGirolamo, N., and Ivanoff, A.: Intersensor Calibration Between F13 SSMI  
28 and F17 SSMIS for Global Sea Ice Data Records, *IEEE Geosci. Remote Sens. Lett.*, 9, 233–236,  
29 10.1109/lgrs.2011.2166754, 2012.
- 30 Dai, L., Che, T., Ding, Y., and Hao, X.: Evaluation of snow cover and snow depth on the Qinghai–  
31 Tibetan Plateau derived from passive microwave remote sensing, *The Cryosphere*, 11, 1933–1948,  
32 10.5194/tc-11-1933-2017, 2017.
- 33 Dai, L., Che, T., Xie, H., and Wu, X.: Estimation of Snow Depth over the Qinghai-Tibetan Plateau Based  
34 on AMSR-E and MODIS Data, *Remote Sensing*, 10, 1989, 10.3390/rs10121989, 2018.
- 35 Davenport, I., Sandells, M., and Gurney, R.: The effects of variation in snow properties on passive  
36 microwave snow mass estimation, *Remote Sensing of Environment*, 118, 168–175,  
37 10.1016/j.rse.2011.11.014, 2012.
- 38 Derksen, C., Walker, A., LeDrew, E., and Goodison, B.: Combining SMMR and SSM/I data for time  
39 series analysis of central North American snow water equivalent, *J. Hydrometeorol.*, 4, 304–316,  
40 10.1175/1525-7541(2003)4<304:CSAIDF>2.0.CO;2, 2003.



- 1 Derksen, C., and Walker, A.: Identification of systematic bias in the cross-platform (SMMR and SSM/I)  
2 EASE-grid brightness temperature time series, *IEEE Trans. Geosci. Remote Sens.*, 41, 910–915,  
3 10.1109/tgrs.2003.812003, 2003.
- 4 Derksen, C., Walker, A., and Goodison, B.: Evaluation of passive microwave snow water equivalent  
5 retrievals across the boreal forest/tundra transition of western Canada, *Remote Sensing of Environment*,  
6 96, 315–327, 10.1016/j.rse.2005.02.014, 2005.
- 7 Derksen, C.: The contribution of AMSR-E 18.7 and 10.7 GHz measurements to improved boreal forest  
8 snow water equivalent retrievals, *Remote Sensing of Environment*, 112, 2701–2710,  
9 10.1016/j.rse.2008.01.001, 2008.
- 10 Derksen, C., Toose, P., Rees, A., Wang, L., English, M., Walker, A., and Sturm, M.: Development of a  
11 tundra-specific snow water equivalent retrieval algorithm for satellite passive microwave data, *Remote  
12 Sensing of Environment*, 114, 1699–1709, 10.1016/j.rse.2010.02.019, 2010.
- 13 Derksen, C., and Brown, R.: Spring snow cover extent reductions in the 2008–2012 period exceeding  
14 climate model projections, *Geophysical Research Letters*, 39, 1–6, 10.1029/2012GL053387, 2012.
- 15 Dozier, J., Bair, E. H., and Davis, R. E.: Estimating the spatial distribution of snow water equivalent in  
16 the world's mountains, *WIREs Water*, 3, 461–474, doi 10.1002/wat2.1140, 2016.
- 17 Dorji, T., Hopping, K., Wang, S., Piao, S., Tarchen, T., and Klein, J.: Grazing and spring snow counteract  
18 the effects of warming on an alpine plant community in Tibet through effects on the dominant species,  
19 *Agric. For. Meteorol.*, 263, 188–197, 10.1016/j.agrformet.2018.08.017, 2018.
- 20 Dressler, K., Leavesley, G., Bales, R., and Fassnacht, S.: Evaluation of gridded snow water equivalent  
21 and satellite snow cover products for mountain basins in a hydrologic model, *Hydrol. Process.*, 20, 673–  
22 688, 10.1002/hyp.6130, 2006.
- 23 Durand, M., and Margulis, S.: Feasibility test of multifrequency radiometric data assimilation to estimate  
24 snow water equivalent, *Journal of Hydrometeorology*, 7, 443–457, 10.1175/jhm502.1, 2006.
- 25 Durand, M., Kim, E., and Margulis, S.: Quantifying uncertainty in modeling snow microwave radiance  
26 for a mountain snowpack at the point-scale, including stratigraphic effects, *IEEE Trans. Geosci. Remote  
27 Sens.*, 46, 1753–1767, 10.1109/tgrs.2008.916221, 2008.
- 28 Fernandes, R., Zhao, H., Wang, X., Key, J., Qu, X., and Hall, A.: Controls on Northern Hemisphere snow  
29 albedo feedback quantified using satellite Earth observations, *Geophys. Res. Lett.*, 36, 1–6,  
30 10.1029/2009gl040057, 2009.
- 31 Foster, J., Chang, A., Hall D.: Comparison of Snow Mass Estimation From a Prototype Passive  
32 Microwave Snow Algorithm, a Revised Algorithm and Snow Depth Climatology, *Remote Sensing of  
33 Environment*, 62, 132–142, 10.1016/S0034-4257(97)00085-0, 1997.
- 34 Foster, J., Hall, D., Eylander, J., Riggs, G., Nghiem, S., Tedesco, M., Kim, E., Montesano, P., Kelly, R.,  
35 Casey, K., and Choudhury, B.: A blended global snow product using visible, passive microwave and  
36 scatterometer satellite data, *International Journal of Remote Sensing*, 32, 41 1371–1395,  
37 10.1080/01431160903548013, 2011.
- 38 Gislason, P., Benediktsson, J., and Sveinsson, J.: Random forests for land cover classification, *Pattern  
39 Recogn. Lett.*, 27, 294–300, 10.1016/j.patrec.2005.08.011, 2006.



- 1 Gong, G., Cohen, J., Entekhabi, D., and Ge, Y.: Hemispheric-scale climate response to Northern Eurasia
- 2 land surface characteristics and snow anomalies, *Glob. Planet. Change*, 56, 359–
- 3 370, 10.1016/j.gloplacha.2006.07.025, 2007.
- 4 Grody, N., Basist, A.: Global identification of snowcover using SSM/I measurements, *IEEE Trans.*
- 5 *Geosci. Remote Sens*, 34, 237–249, 10.1109/36.481908, 1996.
- 6 Hao, S., Jiang, L., Shi, J., Wang, G., Liu, X.: Assessment of MODIS-Based Fractional Snow Cover
- 7 Products Over the Tibetan Plateau, *IEEE Journal of Selected Topics in Applied Earth Observations and*
- 8 *Remote Sensing*, 99, 1-16, 10.1109/JSTARS.2018.2879666, 2018.
- 9 Hernandez-Henriquez, M.A., Dery, S.J., and Derksen, C.: Polar amplification and elevation-dependence
- 10 in trends of Northern Hemisphere snow cover extent, 1971–2014, *Environmental Research Letters*, 10,
- 11 044010, 10.1088/1748-9326/10/4/044010, 2015.
- 12 Hoegh-Guldberg, O., Jacob, D., Taylor, M., Bindi, M., Brown, S., Camilloni, I., Diedhiou, A., Djalante,
- 13 R., Ebi, K., and Engelbrecht, F.: Impacts of 1.5C Global Warming on Natural and Human Systems, IPCC,
- 14 Geneva, Switzerland, 2018.
- 15 Huang, C., Newman, A., Clark M., Andrew, W., and Zheng, X.: Evaluation of snow data assimilation
- 16 using the Ensemble Kalman Filter for seasonal streamflow prediction in the Western United States,
- 17 *Hydrology and Earth System Sciences*, 21, 635-650, 10.5194/hess-21-635-2017, 2017.
- 18 Huang, X., Deng, J., Wang, W., Feng, Q., and Liang, T.: Impact of climate and elevation on snow cover
- 19 using integrated remote sensing snow products in Tibetan Plateau, *Remote Sensing of Environment*,
- 20 37 190, 274-288, 10.1016/j.rse.2016.12.028, 2017.
- 21 Imaoka, K., Takashi, M., Misako, K., Marehito, K., Norimasa, I., and Keizo, N.: Status of AMSR2
- 22 instrument on GCOM-W1, earth observing missions and sensors: Development, implementation, and
- 23 characterization, *International Society for Optics and Photonics*, 10.1117/12.977774, 2012.
- 24 Jiang, L., Shi, J., Tjuatja, S., Dozier, J., Chen, K., and Zhang, L.: A parameterized multiple-scattering
- 25 model for microwave emission from dry snow, *Remote Sensing of Environment*, 111, 357-366,
- 26 10.1016/j.rse.2007.02.034, 2007.
- 27 Jiang, L., Wang, P., Zhang, L., Yang, H., Yang, J.: Improvement of snow depth retrieval for FY3B-
- 28 MWRI in China, *Science China: Earth Sciences*, 44, 531-47, 10.1007/s11430-013-4798-8, 2014.
- 29 Kawanishi, T., Sezai, T., Ito, Y., Imaoka, K., Takeshima, T., Ishido, Y., Shibata, A., Miura, M., Inahata,
- 30 H., and Spencer, R.: The Advanced Scanning Microwave Radiometer for the Earth Observing System
- 31 (AMSR-E): NASA's contribution to the EOS for global energy and water cycle studies, *IEEE Trans.*
- 32 *Geosci. Remote Sens*, 41, 184–194, 10.1109/TGRS.2002.808331, 2003.
- 33 Kelly, R., Chang, A., Leung, T., and Foster, L.: A prototype AMSR-E global snow area and snow depth
- 34 algorithm, *IEEE Transactions on Geoscience and Remote Sensing*, 41, 230 - 242,
- 35 10.1109/TGRS.2003.809118, 2003.
- 36 Kelly, R.: The AMSR-E Snow Depth Algorithm: Description and Initial Results, *Journal of The Remote*
- 37 *Sensing Society of Japan*, 29, 307-317, 10.11440/rssj.29.307, 2009
- 38 Kendall, M. G.: *Rank Correlation Methods*, Griffin, London, 1975.
- 39 Kevin, J., Kotlarski, S., Scherrer, S., and Schär, C.: The Alpine snow-albedo feedback in regional climate
- 40 models, *Climate Dynamics*, 48, 1109–1124, 10.1007/s00382-016-3130-7, 2017.



- 1 Knowles, K., Njoku, E., Armstrong, R., and Brodzik, M.: Nimbus-7 SMMR Pathfinder Daily EASE-  
2 Grid Brightness Temperatures, Version 1. Boulder, Colorado USA. NASA National Snow and Ice Data  
3 Center Distributed Active Archive Center, 10.5067/36SLCSCZU7N6, 2000.
- 4 Larue, F., Royer, A., De, S., Langlois, A., Roy, A., and Brucker, L.: Validation of globsnow-2 snow  
5 water equivalent over eastern canada, *Remote Sensing of Environment*, 194, 264-277,  
6 10.1016/j.rse.2017.03.027, 2017.
- 7 Lemmetyinen, J., Derksen, C., Toose, P., Proksch, M., Pulliainen, J., Kontu, A., Rautiainen, K., and  
8 Seppänen, J.: Hallikainen, M. Simulating seasonally and spatially varying snow cover brightness  
9 temperature using HUT snow emission model and retrieval of a microwave effective grain size, *Remote*  
10 *Sensing of Environment*, 156, 71–95, 10.1016/j.rse.2014.09.016, 2015.
- 11 Lettenmaier, D., Alsdorf, D., Dozier, J., Huffman, G., Pan, M., and Wood, E.: Inroads of remote sensing  
12 into hydrologic science during the WRR era, *Water Resour. Res.*, 51, 7309-7342,  
13 10.1002/2015WR017616, 2015.
- 14 Li, Q., Kelly, R.: Correcting Satellite Passive Microwave Brightness Temperatures in Forested  
15 Landscapes Using Satellite Visible Reflectance Estimates of Forest Transmissivity, *IEEE Journal of*  
16 *Selected Topics in Applied Earth Observations and Remote Sensing*, 10, 3874-3883,  
17 10.1109/JSTARS.2017.2707545, 2017.
- 18 Li, Q., Kelly, R., Leppanen, L., Juho, V., Kontu, A., Lemmetyinen, J., and Pulliainen, J.: The Influence  
19 of Thermal Properties and Canopy-Intercepted Snow on Passive Microwave Transmissivity of a Scots  
20 Pine, *IEEE Transactions on Geoscience and Remote Sensing*, 99, 1-10, 10.1109/TGRS.2019.2899345,  
21 2019.
- 22 Li, X., Liu, Y., Zhu, X., Zheng, Z., and Chen, A.: Snow Cover Identification with SSM/I Data in China,  
23 Liang, J., Liu, X., Huang, K., Li, X., Shi, X., Chen, Y., and Li, J.: Improved snow depth retrieval by  
24 integrating microwave brightness temperature and visible/infrared reflectance, *Remote Sensing of*  
25 *Environment*, 156, 500–509, 10.1016/j.rse.2014.10.016, 2015.
- 26 *Journal of Applied Meteorological Science*, 18, 12-20, 2007.
- 27 Liu, X., Jiang, L., Wu, S., Hao, S., Wang, G., and Yang, J.: Assessment of Methods for Passive  
28 Microwave Snow Cover Mapping Using FY-3C/MWRI Data in China, *Remote Sensing*, 10, 524-539,  
29 10.3390/rs10040524, 2018.
- 30 Liu, X., Jiang, L., Wang, G., Hao, S., and Chen, Z.: Using a Linear Unmixing Method to Improve Passive  
31 Microwave Snow Depth Retrievals, *IEEE J. Sel. Top. Appl. Earth Obs. Remote Sens.*, 11, 4414–4429,  
32 10.1109/PIERS.2016.7735542, 2018.
- 33 Lowe, H., and Picard, G.: Microwave scattering coefficient of snow in MEMLS and DMRT-ML revisited:  
34 the relevance of sticky hard spheres and tomography-based estimates of stickiness, *The Cryosphere*, 9,  
35 2495-2542, 10.5194/tc-9-2101-2015, 2015.
- 36 Luo, J., Pulliainen, J., Takala, M., Lemmetyinen, J., Kangwa, M., Smolander, T., Derksen, C., and  
37 Pinnock, S.: ESA Globsnow: Algorithm Theoretical Basis Document-SWE-algorithm. Technical Report,  
38 European Space Agency (ESA), <http://cedadocs.ceda.ac.uk/id/eprint/1263>, 2013.
- 39 Mann, H. B.: Nonparametric tests against trend, *Econometrica* 13, 245–259, 1945.



- 1 Matzler, C., and Wiesmann, A.: Extension of the microwave emission model of layered snowpacks to  
2 coarse-grained snow, *Remote Sensing of Environment*, 70, 317–325, 10.1016/s0034-4257(99)00047-4,  
3 1999.
- 4 Meier, W., Khalsa, S., and Savoie, M.: Intersensor calibration between F-13 SSM/I and F-17 SSMIS  
5 near-real-time sea ice estimates, *IEEE Trans. Geosci. Remote Sens.*, 49, 3343–3349,  
6 10.1109/tgrs.2011.2117433, 2011.
- 7 Metsämäki, S., Pulliainen, J., Salminen, M., Luojus, K., Wiesmann, A., Solberg, R., Böttcher, K.,  
8 Hiltunen, M., and Ripper, E.: Introduction to GlobSnow Snow Extent products with considerations for  
9 accuracy assessment, *Remote Sensing of Environment*, 156, 96–108, 10.1016/j.rse.2014.09.018, 2015.
- 10 Okuyama, A.; Imaoka, K.: Intercalibration of Advanced Microwave Scanning Radiometer-2 (AMSR2)  
11 Brightness Temperature, *IEEE Trans. Geosci. Remote Sens.*, 53, 4568–4577,  
12 10.1109/MicroRad.2014.6878940, 2015.
- 13 Orsolini, Y., Wegmann, M., Dutra, E., Liu, B., Balsamo, G., Yang, K., de Rosnay, P., Zhu, C., Wang,  
14 W., Senan, R., and Arduini, G.: Evaluation of snow depth and snow cover over the Tibetan Plateau in  
15 global reanalyses using in situ and satellite remote sensing observations, *The Cryosphere*, 13, 2221–2239,  
16 10.5194/tc-13-2221-2019, 2019.
- 17 Pan, J., Durand, M., Sandells, M., Lemmetyinen, J., Kim, E., Pulliainen, J., Koutu, A., and Derksen, C.:  
18 Differences between the HUT snow emission model and MEMLS and their effects on brightness  
19 temperature simulation, *IEEE Trans. Geosci. Remote Sens.*, 54, 2001–2019,  
20 10.1109/TGRS.2015.2493505, 2016.
- 21 Pan, J., Durand, M., Vander Jaqt, B., and Liu, D.: Application of a Markov Chain Monte Carlo algorithm  
22 for snow water equivalent retrieval from passive microwave measurements, *Remote Sensing of*  
23 *Environment*, 192, 150–165, 10.1016/j.rse.2017.02.006, 2017.
- 24 Picard, G.: Simulation of the microwave emission of multi-layered snowpacks using the dense media  
25 radiative transfer theory: The DMRT-ML model, *Geosci. Model Develop. Discuss.*, 6, 3647–3694, 2012.
- 26 Pulliainen, J., Grandell, J., and Hallikainen, M.: HUT snow emission model and its applicability to snow  
27 water equivalent retrieval, *IEEE Trans. Geosci. Remote Sens.*, 37, 1378–1390, 10.1109/36.763302, 1999.
- 28 Pulliainen, J.: Mapping of snow water equivalent and snow depth in boreal and sub-arctic zones by  
29 assimilating space-borne microwave radiometer data and ground-based observations, *Remote Sens.*  
30 *Environ*, 101, 257–269, 10.1016/j.rse.2006.01.002, 2006.
- 31 Qu, Y., Zhu, Z., Chai, L., Liu, S., Montzka, C., Liu, J., Yang, X., Lu, Z., Jin, R., Li, X., Guo, Z., and  
32 Zheng, J.: Rebuilding a Microwave Soil Moisture Product Using Random Forest Adopting AMSR-  
33 E/AMSR2 Brightness Temperature and SMAP over the Qinghai–Tibet Plateau, China, *Remote Sensing*,  
34 11, 683, 10.3390/rs11060683, 2019.
- 35 Rodríguez-Fernández, N., Aires, F., Richaume, P., Kerr, Y., Prigent, C., Kolassa, J., Cabot, F., Jiménez,  
36 C., Mahmoodi, A., and Drusch, M.: Soil Moisture Retrieval Using Neural Networks: Application to  
37 SMOS, *IEEE Trans. Geosci. Remote Sens.*, 53, 5991–6007, 10.1109/TGRS.2015.2430845, 2015.
- 38 Rodríguez-Galiano, V., Ghimire, B., Rogan, J., Chica-Olmo, M., and Rigol-Sanchez, J.: An assessment  
39 of the effectiveness of a random forest classifier for land-cover classification, *ISPRS J. Photogramm.*  
40 *Remote Sens.*, 67, 93–104, 10.1016/j.isprsjprs.2011.11.002, 2012.





- 1 Roy, A., Royer, A., and Hall R.: Relationship Between Forest Microwave Transmissivity and Structural  
2 Parameters for the Canadian Boreal Forest, *IEEE Geoscience and Remote Sensing Letters*, 11, 1802-  
3 1806, 10.1109/LGRS.2014.2309941, 2014.
- 4 Saberi, N., Kelly, R., Toose, P., Roy, A., and Derksen, C.: Modeling the observed microwave emission  
5 from shallow multi-layer tundra snow using DMRT-ML, *Remote Sensing*, 9, 1327, 10.3390/rs9121327,  
6 2017.
- 7 Safavi, H., Sajjadi, S., and Raghbi, V.: Assessment of climate change impacts on climate variables using  
8 probabilistic ensemble modeling and trend analysis, *Theoretical and Applied Climatology*, 130, 635–653,  
9 10.1007/s00704-016-1898-3, 2017.
- 10 Santi, E., Pettinato, S., Paloscia, S., Pampaloni, P., MacElloni, G., and Brogioni, M.: An algorithm for  
11 generating soil moisture and snow depth maps from microwave spaceborne radiometers: HydroAlgo,  
12 *Hydrology and Earth System Sciences*, 16, 3659–3676, 10.5194/hess-16-3659-2012, 2012.
- 13 Takala, M., Luojus, K., Pulliainen, J., Lemmetyinen, J., Juha-Petri, K., Koskinen, J., and Bojkov, B.:  
14 Estimating northern hemisphere snow water equivalent for climate research through assimilation of  
15 space-borne radiometer data and ground-based measurements, *Remote Sensing of Environment*, 115,  
16 3517-3529, 10.1016/j.rse.2011.08.014, 2011.
- 17 Takala, M., Ikonen, J., Luojus, K., Lemmetyinen, J., Metsämäki, S., Cohen, J., Arslan, A., and Pulliainen  
18 J.: New Snow Water Equivalent Processing System With Improved Resolution Over Europe and its  
19 Applications in Hydrology, *IEEE Journal of Selected Topics in Applied Earth Observations and Remote*  
20 *Sensing*, 10, 428-436, 10.1109/JSTARS.2016.2586179, 2017.
- 21 Tedesco, M., and Narvekar, P.: Assessment of the NASA AMSR-E SWE product, *IEEE Journal of*  
22 *Selected Topics in Applied Earth Observations and Remote Sensing*, 3, 141-159,  
23 10.1109/jstars.2010.2040462, 2010.
- 24 Tedesco, M. and Jeyaratnam, J.: A new operational snow retrieval algorithm applied to historical AMSR-  
25 E brightness temperatures, *Remote Sensing*, 8, 1037, 10.3390/rs8121037, 2016.
- 26 Tsai, Y., Dietz, A., Oppelt, N., Kuenzer, C.: Wet and Dry Snow Detection Using Sentinel-1 SAR Data  
27 for Mountainous Areas with a Machine Learning Technique, *Remote Sensing*, 11, 895,  
28 10.3390/rs11080895, 2019.
- 29 Wang, J., Che, T., Li, Z., Li, H., Hao, X., Zheng, Z., Xiao, P., Li, X., Huang, X., Zhong, X., Dai, L., Li,  
30 H., Ke, C., and Li, L.: Investigation on snow characteristics and their distribution in China, *Advances in*  
31 *Earth Science*, 33, 12-26, 10.11867/j.issn.1001-8166.2018.01.0012, 2018.
- 32 Wang, Y., Huang, X., Wang, J., Zhou, M., and Liang, T.: AMSR2 snow depth downscaling algorithm  
33 based on a multifactor approach over the Tibetan Plateau, China, *Remote Sensing of Environment*, 231,  
34 1-14, 10.1016/j.rse.2019.111268, 2019.
- 35 Xiao, X., Zhang, T., and Zhong, X.: Support vector regression snow-depth retrieval algorithm using  
36 passive microwave remote sensing data, *Remote Sensing of Environment*, 210, 48-64,  
37 10.1016/j.rse.2018.03.008, 2018.
- 38 Xiao, X., Zhang, T., Zhong, X., Li, X., and Li, Y.: Spatiotemporal variation of snow depth in the Northern  
39 Hemisphere from 1992 to 2016, *The Cryosphere Discuss.*, <https://doi.org/10.5194/tc-2019-33>, in review,  
40 2019.



- 1 Yang, H., Weng, F., Lv, L., Lu, N., Liu, G., Bai, M., Qian, Q., He, J., and Xu, H.: The FengYun-3
- 2 microwave radiation imager on-orbit verification, *IEEE Trans. Geosci. Remote Sens.*, 49, 4552–4560,
- 3 10.1109/tgrs.2011.2148200, 2011.
- 4 Yang, J., Jiang, L., Ménard, C., Luo, J., Lemmetyinen, J., and Pulliainen, J.: Evaluation of snow
- 5 products over the Tibetan Plateau, *Hydrol. Processes*, 29, 3247–3260, 10.1002/hyp.10427, 2015.
- 6 Yang, J., Jiang, L., Wu, S., Wang, G., Wang, J., and Liu, X.: Development of a Snow Depth Estimation
- 7 Algorithm over China for the FY-3D/MWRI, *Remote Sensing*, 11, 977, 10.3390/rs11080977, 2019.
- 8 Zhong, X., Zhang, T., Kang, S., Wang, K., Zheng, L., Hu, Y., and Wang, H.: Spatiotemporal variability
- 9 of snow depth across the Eurasian continent from 1966 to 2012, *The Cryosphere*, 12, 227–245,
- 10 10.5194/tc-12-227-2018, 2018.

11

12 **List of Tables and Figures**

13 Table 1. Summary of the main passive microwave remote sensing sensors.

Sensor	SMMR	SSM/I		SSM/I/S		AMSR-E	AMSR2	MWRI		
Satellite	Nimbus-7	DMSF-F08	DMSF-F11	DMSF-F13	DMSF-F17	EOS Aqua	GCOM-W	FY-3B	FY-3C	FY-3D
On Orbit time	1978-1987	1987-1991	1991-1995	1995-2008	2006-present	2002-2011	2012-present	2010-present	2013-present	2017-present
Passing Time	A: 12:00 D: 24:00	A: 06:20 D: 18:20	A: 17:17 D: 05:17	A: 17:58 D: 05:58	A: 17:31 D: 05:31	A: 01:30 D: 13:30	A: 01:30 D: 13:30	A: 13:30 D: 01:30	A: 22:00 D: 10:00	A: 14:00 D: 02:00
Frequency:	6.6: 95×160		19.35: 45×68		19.35: 42×70	6.925: 43×75 10.65: 29×51	6.925: 35×62 7.3: 35×62		10.65: 51 × 85	
Footprint (GHz):	10.7: 60×100		23.235: 40×60		23.235: 42×70	18.7: 16× 27	10.65: 24×42		23.8: 27 × 45	
(km × km)	18: 35×60		37: 24×36		37: 28×44	23.8: 18×32	18.7: 14× 22		36.5: 18 × 30	
	21: 30×50		85.5: 11×16		91.655: 13×15	36.5: 8×14	23.8: 15×26		89: 9 × 15	
	37: 17×29					89: 4×6	36.5: 7×12			
							89: 3×5			

14

15 Table 2. Details of the snow field sampling data (location, attitude, altitude and land cover type).

Snow sampling pixels in Xinjiang					Snow sampling pixels in Northeast China				
No	longitude	latitude	altitude (m)	land cover	No	longitude	latitude	altitude (m)	land cover
1	84.026	42.973	2400	grass	1	125.514	44.765	186	farm
2	84.047	42.977	2431	grass	2	125.434	44.762	195	farm
3	84.069	42.983	2436	grass	3	125.434	44.717	179	farm
4	84.094	42.988	2444	grass	4	125.512	44.722	181	farm
5	84.117	42.994	2389	grass	5	125.480	44.680	154	farm
6	84.128	43.003	2408	grass	6	125.509	44.678	164	farm
7	84.127	43.014	2415	grass	7	125.435	44.673	178	farm
8	84.134	43.021	2412	grass	8	125.442	44.634	160	farm
9	84.172	43.036	2415	grass	9	125.506	44.632	159	farm
10	84.201	43.047	2432	grass	10	125.373	44.768	196	farm
11	84.229	43.055	2408	grass	11	125.300	44.766	194	farm
12	84.263	43.058	2425	grass	12	125.299	44.727	207	farm



13	84.286	43.061	2431	grass	13	125.375	44.724	176	farm
14	84.131	43.000	2412	grass	14	125.365	44.681	192	farm
15	84.129	42.988	2430	grass	15	125.344	44.680	195	farm
16	84.142	42.973	2470	grass	16	125.313	44.650	206	farm
17	84.142	42.989	2450	grass	17	125.291	44.586	188	farm
18	84.170	42.933	2520	grass	18	125.361	44.588	165	farm
19	84.189	42.912	2510	grass	19	125.450	44.584	158	farm
20	84.188	42.914	2510	grass	20	125.517	44.585	162	farm
21	84.217	42.887	2470	grass	21	125.370	44.625	185	farm
22	84.218	42.887	2500	grass					
23	84.234	42.872	2450	grass					
24	84.250	42.851	2420	grass					
25	84.266	42.858	2480	grass					
26	84.266	42.858	2440	grass					

1

2 Table 3. Predictor and target variables of the RF model

Name	Description	Number
<b>Predictors</b>		
10.65 GHz		
18.7 GHz	AMSR2 brightness temperature at V and H	8
36.5 GHz	polarizations	
89 GHz		
Grass		
Farm		
Forest	Land cover fraction ranging from 0 to 100	5
Shrub	retrieved from 1-km LULC map	
Barren		
Latitude (°)	Geolocation of weather station	2
Longitude (°)		
<b>Target</b>		
SD (cm)	Station snow depth	1

3

4 Table 4. Summary of land cover effects on the reconstructed product accuracy.

Land Cover Types	RMSE (cm)	Bias (cm)	Correlation ( $R^2$ )	Samples
Forest	6.2	-0.81	0.43	2680
Grass	5.5	-0.18	0.74	2763
Farm	4.2	0.51	0.58	5255
Barren	4.6	0.71	0.35	553

5

6

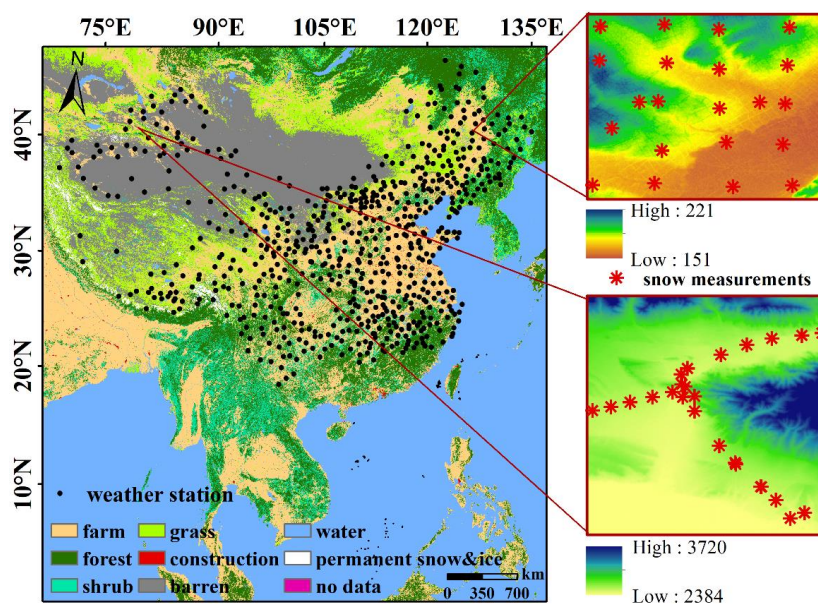
7



1 Table 5. The main input parameters of MEMLS.

Ranges and steps of variables used for the simulation of TB by MEMLS				
Items	Snow Depth	Snow Density	Correlation Length	Snow-ground Reflectivity
Range	1~100 cm	50~400 kg m <sup>-3</sup>	0.01~0.5 mm	H-polarization: 0.2
Interval	1 cm	10 kg m <sup>-3</sup>	0.05 mm	V-polarization: 0.07
The constant values of snow parameters used for the simulation of TB by MEMLS				
Items	Liquid Water Content	Salinity	Incidence Angle	Ground & Snow Temperature
Value	0	0	55°	270 K

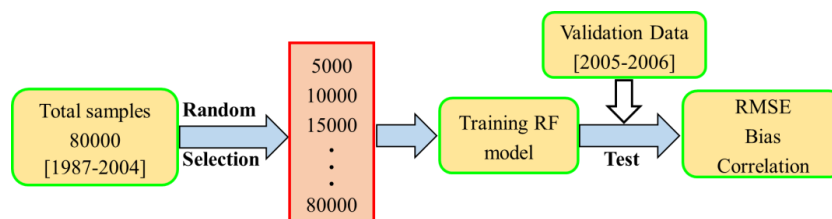
2



3

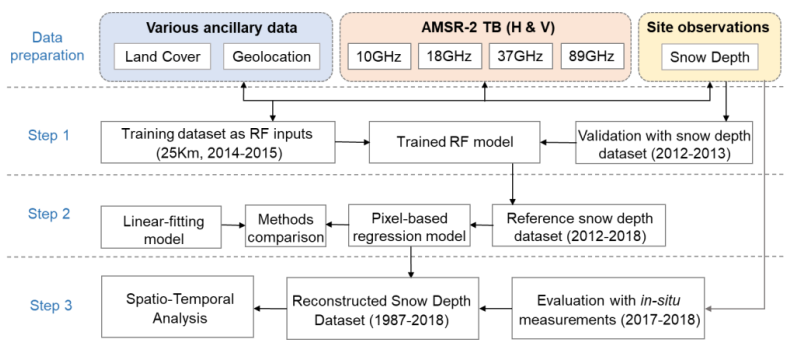
4 Figure 1. Spatial distribution of the weather stations and land cover types in study area. Black points are  
 5 station sites where snow depth recorded is greater than 0 cm. Right attached figures describe the  
 6 configuration of the snow sampling experiment. The red marker represents the snow sampling points  
 7 within one pixel (25 × 25 km<sup>2</sup>). There are 26 and 21 snow measurements in Xinjiang and Northeast China,  
 8 respectively.

9



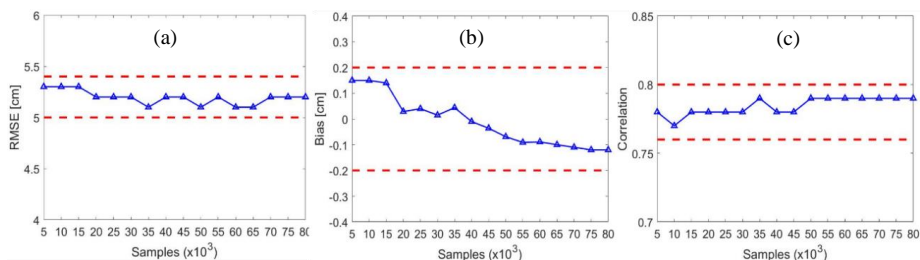
10

11 Figure 2. The test process flowchart for the RF model.



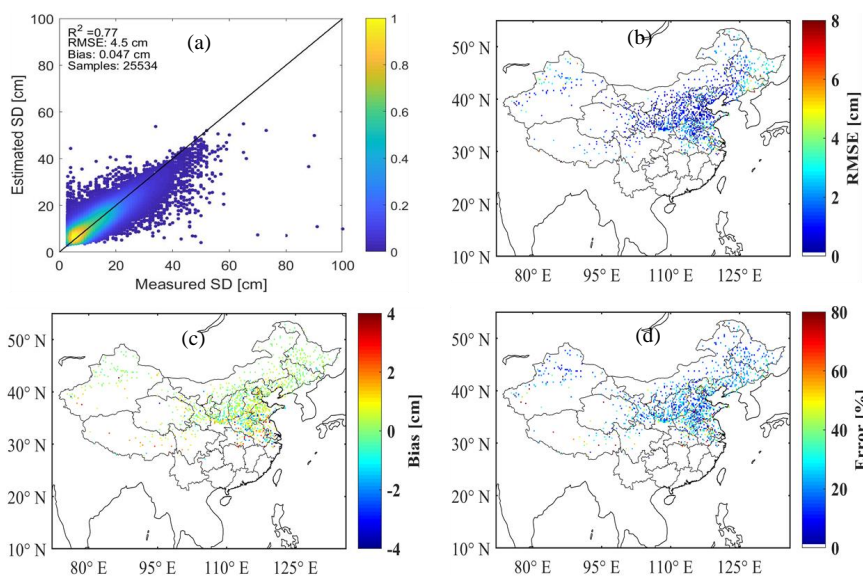
1  
 2 Figure 3. Flowchart of the snow depth reconstruction in this study.

3



4  
 5 Figure 4. RF stability for the numbers of training samples: (a) RMSE; (b) bias and (c) correlation  
 6 coefficient.

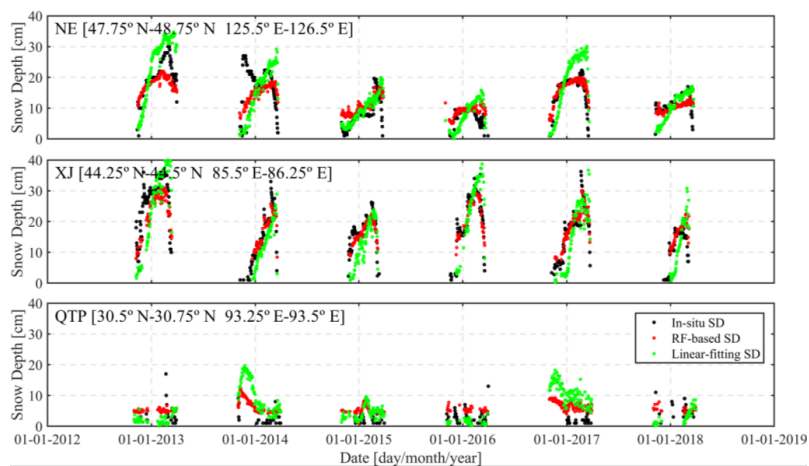
7



8  
 9 Figure 5. Validation of trained RF model: (a) scatterplots, (b) RMSE [cm], (c) bias [cm], and (d) relative  
 10 Error [%].



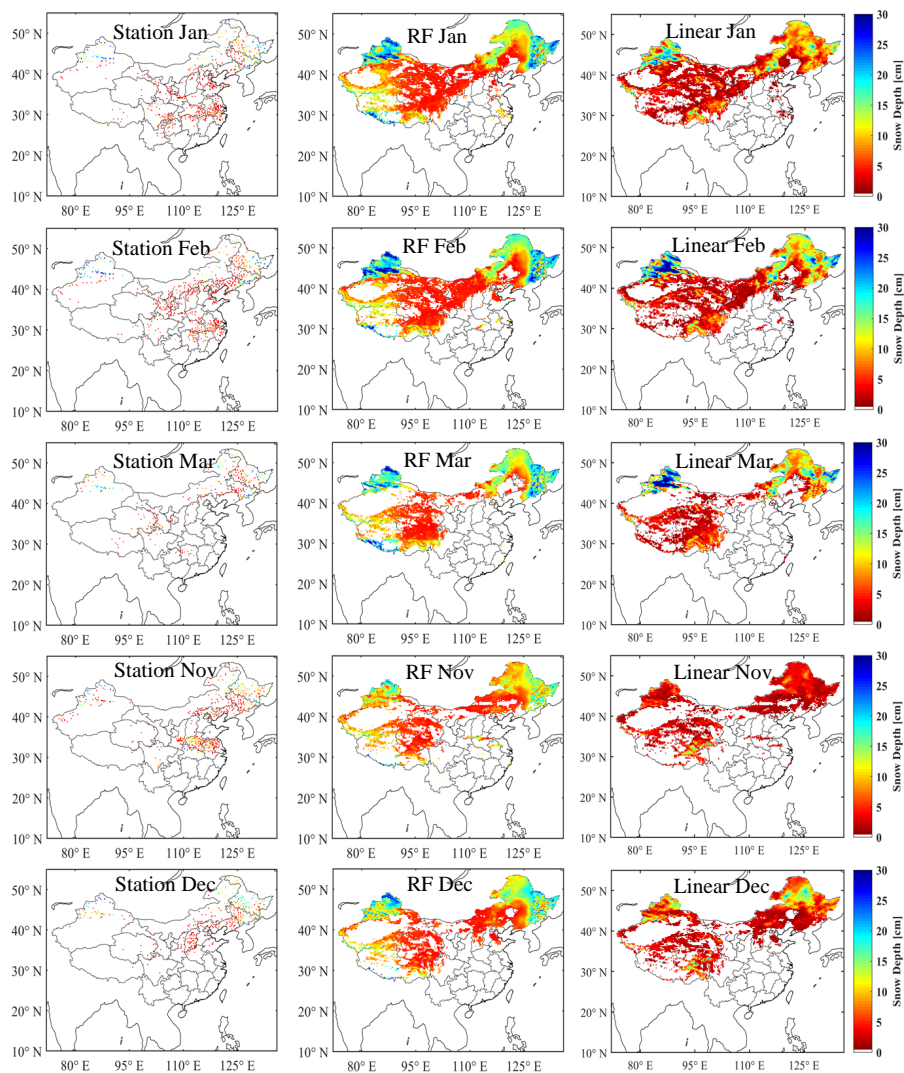
1



2

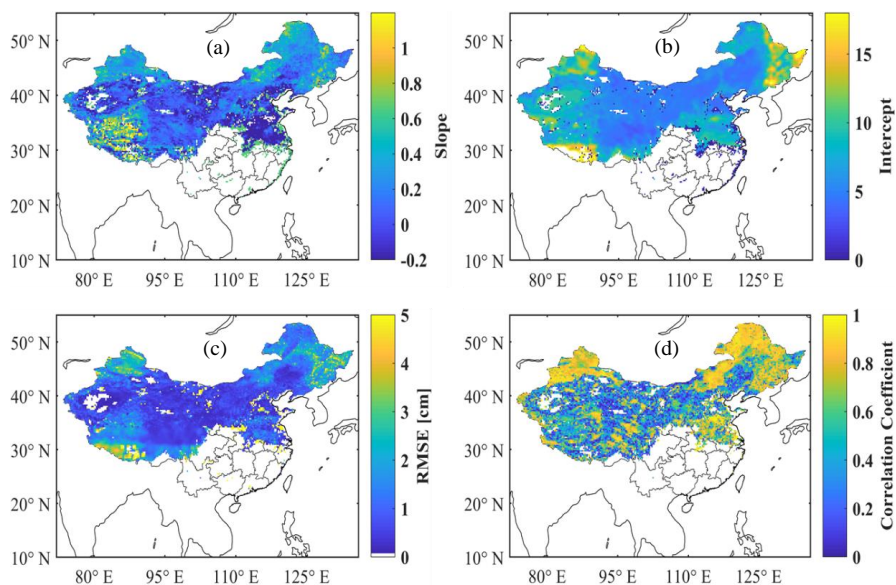
3 Figure 6. Snow depth comparison during winter seasons for the 2012-2018 period. Green dot: RF model;  
4 red dot: linear-fitting model; black dot: station observations. There are sixteen pixels (Northeast China,  
5 NE), three pixels (Xinjiang, XJ) and one pixel (QTP) in the three regions.



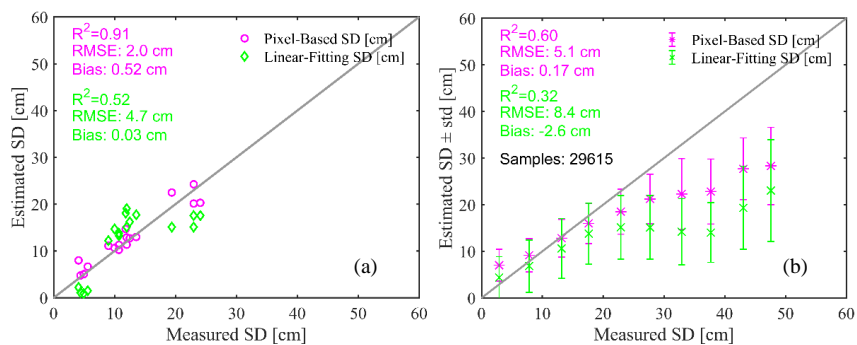


1  
2 Figure 7. Spatial distribution of the monthly mean snow depth for January (Jan, first row), February (Feb,  
3 second row), March (Mar, third row), November (Nov, fourth row), and December (Dec, fifth row), 2016.  
4 Left: Station observations; Middle: RF estimations; Right: linear-fitting retrievals. The color scale  
5 denotes snow depth in centimeters, which ranges from 0 to 30 cm.

6

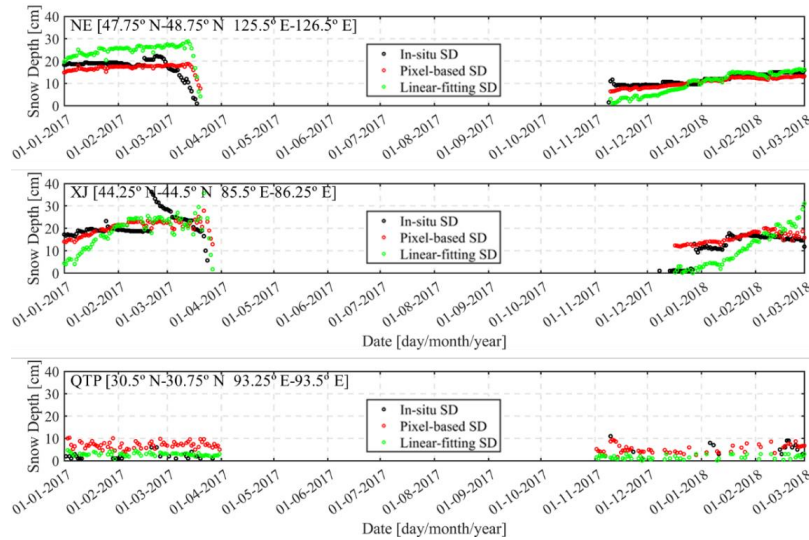


1  
 2 Figure 8. Spatial distribution of pixel-based coefficients: (a) *Slope*; (b) *Intercept*; (c) RMSE; and (d)  
 3 correlation coefficient. The RMSE and correlation coefficient are calculated with the reference snow  
 4 depths and retrievals of the pixel-based method.

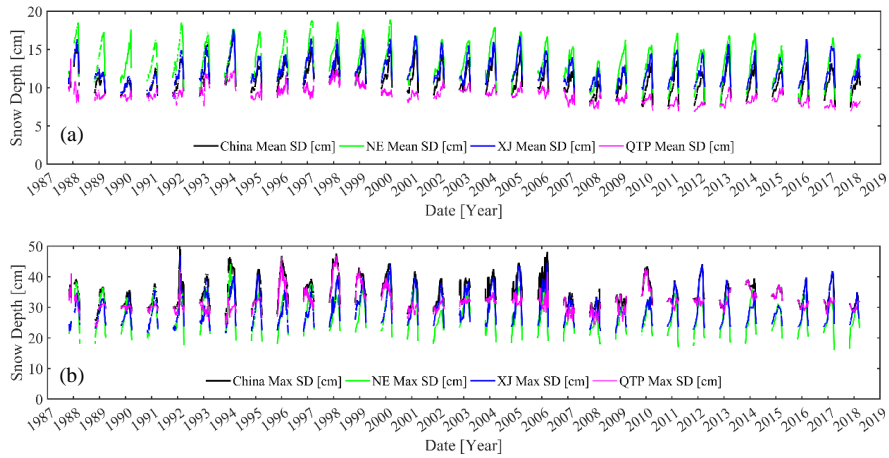


6  
 7 Figure 9. Pixel-based method validation with two sources: (a) field sampling and (b) weather stations.  
 8 Green and magenta markers denote linear-fitting method and pixel-based model, respectively.

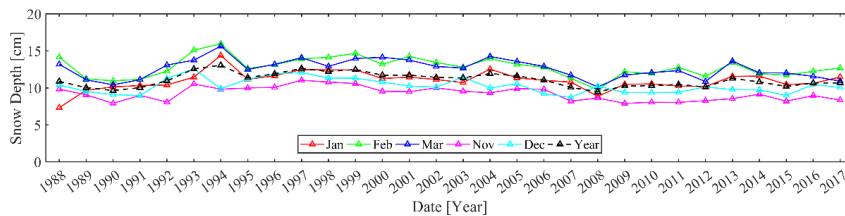




1  
 2 Figure 10. Snow depth validation during the winter seasons for the 2017-2018 period. Black dots: station  
 3 observations; red dots: pixel-based model; green dots: linear-fitting model.  
 4



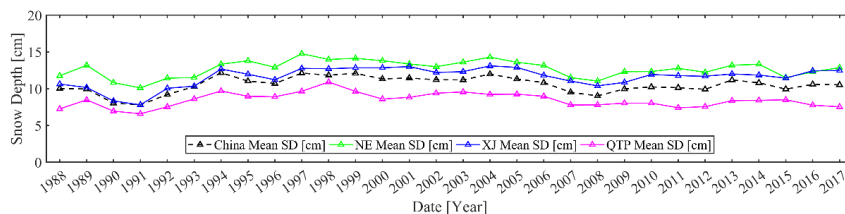
5  
 6  
 7 Figure 11. The time series of snow depth over China during winter seasons: (a) mean snow depth and (b)  
 8 max snow depth. NE: Northeast China; XJ: Xinjiang; QTP: Qinghai-Tibetan Plateau.



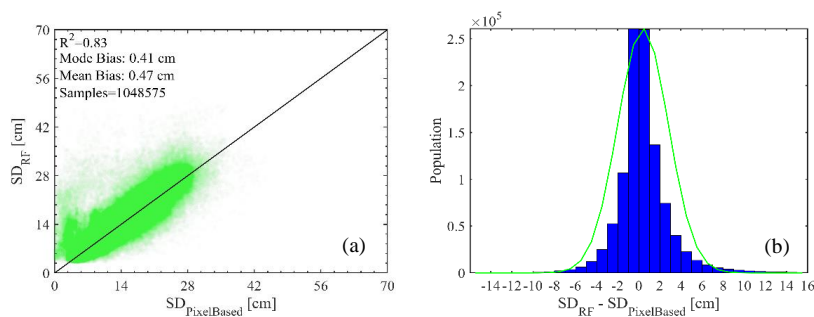
9



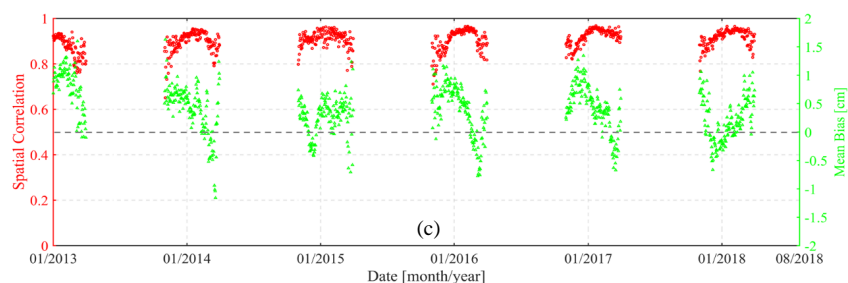
1 Figure 12. Time series of annual mean snow depth over China for the winter seasons. Black dashed line:  
 2 yearly; Red line: January (Jan); Green line: February (Feb); Blue line: March (Mar); Magenta line:  
 3 November (Nov); and Cyan line: December (Dec).

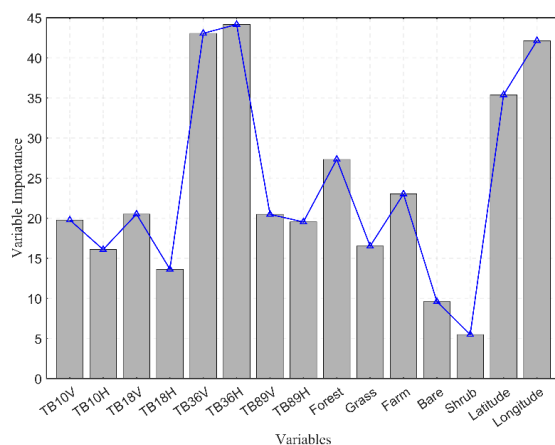


4  
 5 Figure 13. Long-term annual mean snow depth over different subregions. Black dashed line: China;  
 6 Green line: Northeast China, NE; Blue line: Xinjiang, XJ; and Magenta line: QTP.

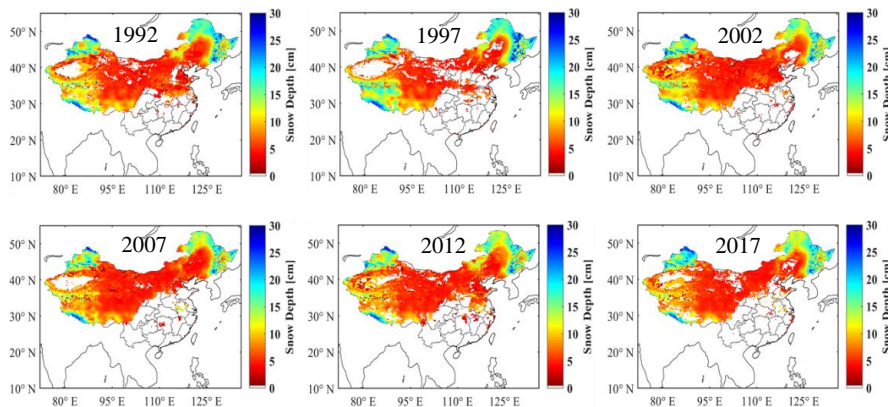


7  
 8  
 9 Figure 14. Comparison of retrievals between the RF model and pixel-based method: (a) scatter plot of  
 10 snow depth; (b) histogram of bias,  $SD_{RF} - SD_{PixelBased}$ ; and (c) temporal series of spatial correlation and  
 11 mean bias. The histogram bin width is 1 cm.

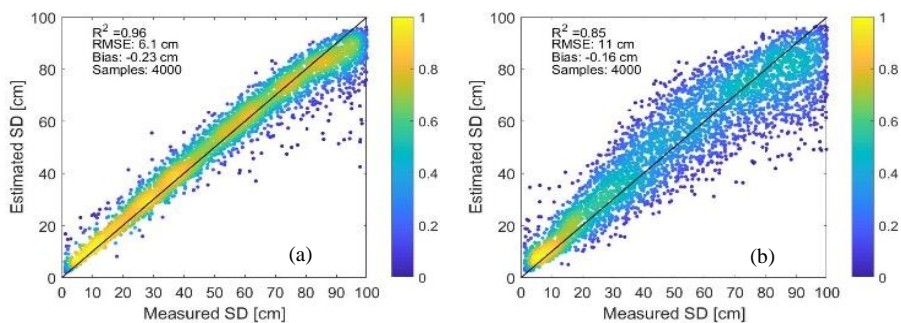




1  
 2 Figure 15. Predictor importance of the RF model based on increased mean square error. The variable  
 3 importance is based on the concept that a variable associated with a considerable reduction in prediction  
 4 accuracy is excluded. The larger the MSE, the greater the importance of the variable is.



5  
 6 Figure 16. Reconstructed annual mean snow depth for 1992-2017 at five-year intervals.



7  
 8 Figure 17. The performance of RF with two validation datasets from the MEMLS model: (a) 10-89 GHz  
 9 brightness temperatures, snow depth, snow density and correlation length; and (b) 10-89 GHz brightness  
 10 temperatures and snow depth. The color scale represents the data density of scattered points, which range  
 11 from 0 to 1.